nature biotechnology

Article

https://doi.org/10.1038/s41587-025-02772-z

Antibody–bottlebrush prodrug conjugates for targeted cancer therapy

Received: 12 November 2024

Accepted: 10 July 2025

Published online: 09 September 2025

Check for updates

Bin Liu[1,2,3], Hung V.-T. Nguyen[1,4,5], Yivan Jiang[4], Aiden X. Wang[1], Valerie Lensch[1], Zehao Sun[6], Zane H. Boyer[7], Philip A. Raftopoulos[7], Yutong Dai[1], Piper L. MacNicol[1], Yuyan Wang[1], Nidhi Jyotsana[8], Wencong Wang[1], Sachin Bhagchandani[1,2], Sanjana Hemdev[4], Peyton Shieh[1], Samantha L. Kristufek[1], Magalie Boucher[9], Michael Downes[8], Ronald M. Evans[8], David W. C. MacMillan[7] & Jeremiah A. Johnson[1,2,10]

Antibody–drug conjugates (ADCs) are effective targeted therapeutics but are limited in their ability to incorporate less-potent payloads, varied drug mechanisms of action, different drug release mechanisms and tunable drug-to-antibody ratios. Here we introduce a technology to overcome these limitations called 'antibody–bottlebrush prodrug conjugates' (ABCs). An ABC consists of an IgG1 monoclonal antibody covalently conjugated to the terminus of a compact bivalent bottlebrush prodrug that has payloads bound through cleavable linkers and polyethylene glycol branches. This design enables the synthesis of ABCs with tunable average drug-to-antibody ratios up to two orders of magnitude greater than those of traditional ADCs. We demonstrate the functional flexibility and manufacturing efficiency of this technology by synthesizing more than 10 different ABCs targeting either HER2 or MUC1 using drugs with potencies spanning several orders of magnitude as well as imaging agents for ABC visualization and photocatalysts for proximity-based labeling of the ABC interactome. ABCs display high target engagement, high cell uptake and improved efficacy in tumor models compared to conventional HER2-targeted ADCs, suggesting promise for clinical translation.

Cancer is a leading cause of death worldwide, and although many transformative cancer therapies have been developed in recent decades, the number of cancer deaths continues to increase, motivating the search for novel targeted therapies[1]. Among the targeted therapy platforms in development for cancer treatment, ADCs, which consist of a monoclonal antibody (mAb) conjugated to a small-molecule drug through a covalent linker, have demonstrated clinical success and future potential[2–13]. More than a dozen ADCs have been approved worldwide and hundreds of ADCs are in preclinical/clinical development[13–18]. Despite these successes[5,19,20], traditional ADCs face inherent limitations that may hinder their broader applicability and versatility[21,22]. The 'payload scope' of ADCs is limited to highly potent cytotoxic agents with few mechanisms of action (MoAs)—for example, microtubule inhibition and DNA damage. As a result, ADCs can display substantial toxicities and developed drug resistance[23,24], which could be resolved with the use of inherently more selective payloads, payload MoAs or payload combinations. Because the payloads of ADCs are directly conjugated to amino acid sidechains of the mAb through linkers with limited functionality,

[1]Department of Chemistry, Massachusetts Institute of Technology, Cambridge, MA, USA. [2]Koch Institute for Integrative Cancer Research, Massachusetts Institute of Technology, Cambridge, MA, USA. [3]Research Laboratory of Electronics, Massachusetts Institute of Technology, Cambridge, MA, USA. [4]Window Therapeutics, Boston, MA, USA. [5]Thayer School of Engineering, Dartmouth College, Hanover, NH, USA. [6]Department of Materials Science and Engineering, Massachusetts Institute of Technology, Cambridge, USA. [7]Merck Center for Catalysis at Princeton University, Princeton, NJ, USA. [8]Gene Expression Laboratory, Salk Institute for Biological Studies, La Jolla, CA, USA. [9]Division of Comparative Medicine, Massachusetts Institute of Technology, Cambridge, MA, USA. [10]Broad Institute of MIT and Harvard, Massachusetts Institute of Technology, Cambridge, MA, USA. e-mail: jaj2109@mit.edu

the average number of payloads that can be conjugated per mAb (that is, the drug-to-antibody ratio (DAR)) before deterioration of ADC properties is currently limited to ≤8 (Fig. 1a)[10–14,21,22,25–29]. Although a higher DAR may not always be better from a therapeutic perspective, particularly when highly potent payloads are used[30], it may be required for ADCs to use payloads that are approximately 10–100-fold less potent than traditional ADC payloads while maintaining a practical mAb dose (for example, all clinically used ADCs so far are given at approximately 1–10 mg kg^{-1} doses of mAb).

Accessing tunable and ultra-high DAR values with a well-defined molecular system that does not preclude mAb function may allow the use of payloads with varied MoAs and antigen targets in a tunable, modular fashion. Attachment or encapsulation of payloads into polymers or nanoparticles that are then conjugated to antibodies is a promising way to achieve this goal (Fig. 1b); however, such designs often lack payload and linker versatility due to the surface-exposed nature of the payloads, which inextricably link the physical properties of the payload–linker to the physical properties of the overall construct[31,32]. A design that facilitates straightforward access to antibody-targeted delivery constructs with predictable physical properties regardless of payload and linker identity could broaden the landscape for cancer therapeutics.

We explored the use of molecular bottlebrush prodrugs (BPDs)[33–37] as a solution to this challenge. BPDs are synthetic polymers with mAb-like dimensions (approximately 10-nm diameter and controlled length) that feature branched pendants containing a hydrophilic polymer chain (for example, polyethylene glycol (PEG)) and a payload–linker unit attached to a compact polymer backbone. The PEG chains of BPDs shield the payload–linker units, which confers consistent physical properties to the BPD regardless of the payload–linker composition and backbone length[8–11]. Moreover, the average number of PEG–payload–linker units, which determines the DAR after mAb conjugation, can be readily varied from approximately 10–100 by controlling the BPD synthesis stoichiometry. Additionally, the microstructure of BPDs enables chemical differentiation of the BPD backbone ends from the PEG surface, which we leverage here to introduce a single 'click' chemistry[38–41] functional group for high-yielding conjugation to one mAb molecule per BPD. In summary, the efficiency of BPD synthesis facilitates the use of a wide range of payloads, linkers and antibodies to optimize ABCs for different disease contexts[35–37].

Here we report the synthesis and evaluation of ABCs in vitro and in vivo (Fig. 1c). First, we develop a synthetic method to terminate the ends of BPDs with reactive handles for selective and efficient 'click' bioconjugation to mAbs using either stochastic (Lys) or site-specific (Cys) methods (Fig. 1c). Then, we demonstrate the synthesis and in vitro and in vivo evaluation of ABCs based on six payload–linker combinations with distinct MoAs and two mAbs that target tumor antigens (HER2 and MUC1). We show that ABCs can have high target-specific engagement and cell uptake with average DAR values up to 135, which leads to higher efficacy compared to non-targeted BPDs and clinical HER2-targeted ADCs despite having payloads that are up to approximately 100-fold less potent. Interactome micromapping experiments, enabled by the installation of photosensitizers into ABCs, show that ABCs engage their expected antigen targets in vitro. ABCs achieve good tumor regression with no discernable toxicities in several in vivo efficacy studies using $HER2^+$ and $MUC1^+$ cell-line-derived xenograft murine models. Moreover, ABCs with SN-38 payloads and a DAR of 60 display improved efficacy in a low-antigen-expressing tumor model compared to T-DXd, an Enhertu biosimilar with a DAR of approximately 8, at the same mAb dose and with a clinically relevant payload dose.

Results

Synthesis of ABCs via a modular 'click' chemistry approach

Our strategy for the synthesis of ABCs involves conjugation of a presynthesized BPD to a mAb (Fig. 1c). We recognized the challenges of coupling nanoscale objects of similar sizes under the mild conditions and low reaction concentrations needed for mAb functionalization. Moreover, the chosen conjugation reaction must be compatible with BPD synthesis and a wide range of payload and linker compositions. 'Click' chemistry reactions have been developed precisely to tackle such challenges[38–41]. We tested various possible methods for installation of 'click' chemistry-compatible functional groups onto the ends of model BPs (lacking payloads and linkers) with polynorbornene backbones (number-average degrees of polymerization = 60) and PEG sidechains with molecular weights of 3,000 (total bottlebrush number-average molecular weight = 200,000) (see supplementary information for discussion: Supplementary Schemes 1–4 and Supplementary Figs. 1 and 2). A versatile protocol was identified wherein BP synthesis via ring-opening metathesis polymerization (ROMP) of suitable macromonomers (Fig. 1d) is quenched by an enyne terminator bearing a 6-methyl-1,2,4,5-tetrazine (enyne-PEG_{12}-Tz; Supplementary Schemes 3 and 4)[42,43], yielding a BP ('BP-Tz') with a single tetrazine on its backbone end (Fig. 1c and Supplementary Fig. 3). BP-Tz is set up for coupling to a *trans*-cyclooctene (TCO)-functionalized mAb via inverse electron demand Diels–Alder cycloaddition, one of the most efficient biorthogonal 'click' reactions[44–46]. As a proof of concept, we first appended TCOs to serum IgG1 via a lysine amidation reaction to provide IgG1-TCO. Notably, mixing BP-Tz and IgG1-TCO together (3:1) in neutral PBS at room temperature for 24 hours gave quantitative consumption of IgG1-TCO to form conjugates PEG-IgG1 as a mixture of species with different numbers of BPs per mAb, as determined by SDS-PAGE gel electrophoresis (Supplementary Fig. 4).

Fig. 1 | Construction and in vitro evaluation of ABCs. a, Traditional ADCs feature DARs of approximately 2–8. **b**, ADCs based on linear polymer–drug conjugates with drugs distributed on the pendants of hydrophilic polymer chains were developed. The surface exposure of payloads and chemical heterogeneity in such systems may limit DAR and payload diversity. **c**, Formation of ABCs through 'click' conjugation between Ab-TCO and BP-Tz enabled by a ROMP terminator (enyne-PEG_{12}-Tz). ABCs comprise a mAb covalently conjugated to the end of one or more BPDs (BAR = 1 shown in figure), the latter of which has hydrophilic polymer chains (blue; PEG in this work), drugs (green) and cleavable linkers (pink) attached to backbone repeat units, leading to a compact, homogenous microstructure that enables DAR values up to approximately 135 for a wide range of mechanistically distinct payloads. **d**, Chemical structures of the six different dye and drug–linker-containing macromonomers used in this work. **e**, Non-reducing SDS-PAGE gel comparing ABCs with different payloads. **f**, Non-reducing SDS-PAGE gel for isolated ABCs with different BAR values. **g**, Binding affinities of various HER2-targeted ADCs and ABCs as measured by MST. ABC30-1 refers to an ABC with DAR = 30 and BAR = 1. ABC60-1 refers to an ABC with DAR = 60 and BAR = 1. Results are presented as mean ± s.e.m. (n = 3 technical replicates). **h**, In vitro characterization of the BT-474 cell-targeting ability of ABCs as measured by flow cytometry (25 μg ml^{-1} ABC, 1-hour incubation, 5% Cy5.5-labeled ABC with BAR = 1). The $x$axis represents the Cy5.5 fluorescence intensity. **i**, Cytotoxicity assay (MTT) comparing ABC MMAE-HER2 and BPD MMAE-BP after 24-hour incubation, showing greater potency for the HER2-targeted ABC. Results are presented as mean ± s.e.m. (n = 3 biological replicates). **j**, Confocal microscopy image showing BT-474 cell binding and uptake of Cy5.5-HER2 (50 μg ml^{-1}, 6-hour incubation, 1% Cy5.5-labeled ABC). Magenta is Cy5.5; blue is Hoechst staining of the nucleus. **k**, Label-free quantitative proteomics for analyzing the targeted interactome of PEG-$HER2^{Ir}$ against an isotype PEG-$IgG1^{Ir}$ ABC on BT-474 cells. Three biological replicates were created for each condition. In such constructs, the Ir-containing photocatalyst was conjugated to the antibodies (trastuzumab or IgG1) via NHS ester–lysine coupling. Then, the PEG-BP was conjugated onto these antibodies to provide PEG-$HER2^{Ir}$ and PEG-$IgG1^{Ir}$ ABCs. Previously reported interactors of HER2 are identified in burgundy, with dashed lines indicating the statistical cutoff of $\log_2$(fold change) > 0.5 and −log(Pvalue) > 1.3. Normalization was performed via median subtraction, and a volcano plot was generated using a t-test for statistical significance. Contaminants were filtered manually for image clarity.

https://doi.org/10.1038/s41587-025-02772-z

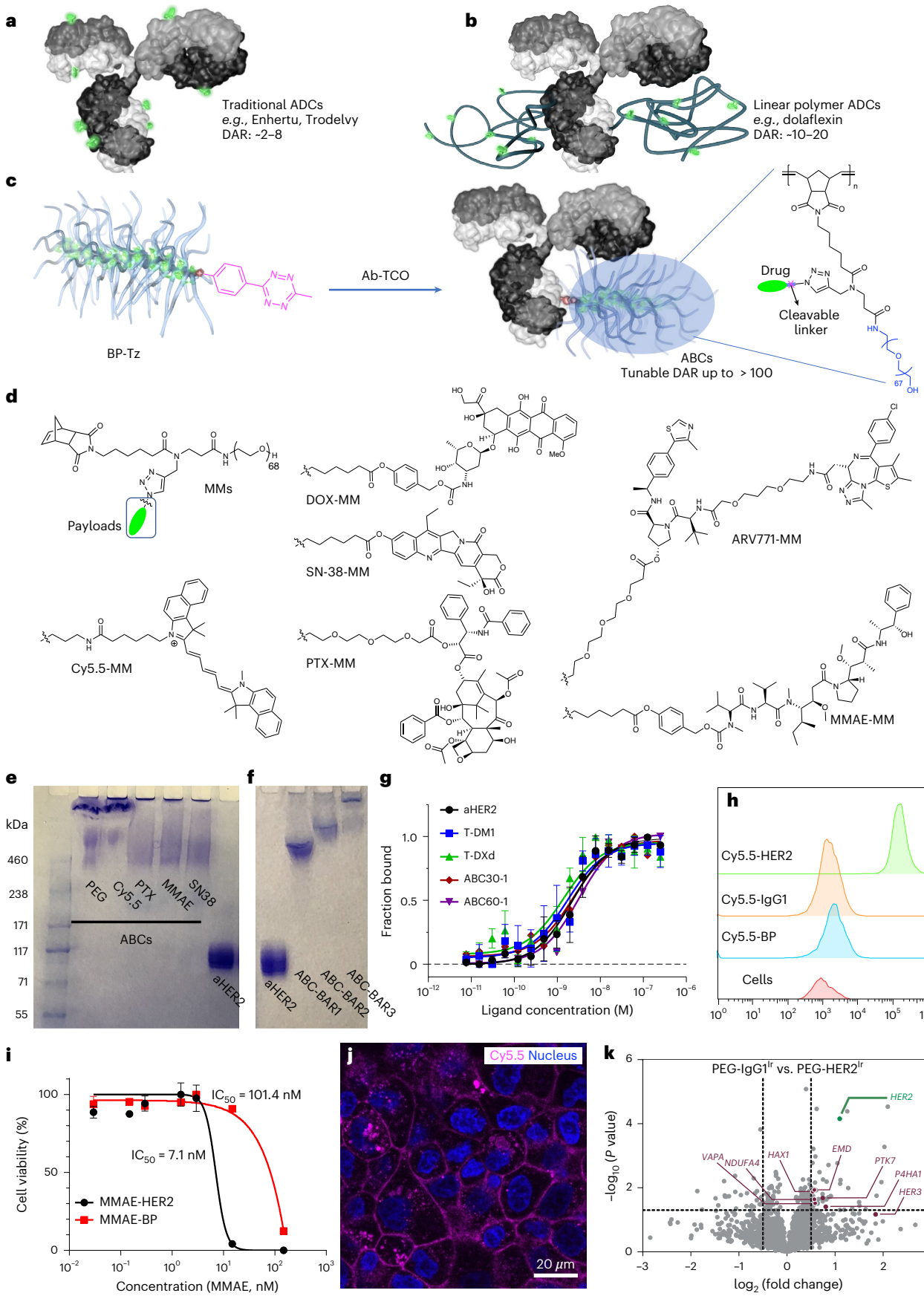

Encouraged by these results, we studied the conjugation of BP-Tz to the HER2-targeting mAb trastuzumab, which is currently used as a therapeutic mAb (Herceptin) and is the basis of clinically approved ADCs such as Kadcyla and Enhertu[47]. Amidation of trastuzumab with TCO gave HER2-TCO (Supplementary Fig. 5), which was subsequently coupled to BP-Tz under the same conditions as described above to provide BP-HER2, as confirmed by SDS-PAGE (Fig. 1e). Next, we synthesized a Tz-terminated, cyanine-5.5 (Cy5.5) dye-labeled BP (Cy5.5-Tz) and three Tz-terminated BPDs with different drugs—paclitaxel (PTX-Tz), monomethylauristatin (MMAE-Tz) and SN-38 (SN-38-Tz); SDS-PAGE showed consumption of HER2-TCO within 24 hours of exposure to each of these constructs (Fig. 1e), providing fluorophore-labeled Cy5.5-HER2 and ABCs PTX-HER2, MMAE-HER2 and SN-38-HER2, respectively[48].

In ABCs, the DAR is determined by the BPD backbone degrees of polymerization as well as the average number of BPDs per mAb (herein referred to as the 'BPD-to-antibody ratio' (BAR)). We hypothesized that BAR could be controlled by varying the conjugation reaction stoichiometry and that the steric hindrance of coupling a second or third bottlebrush to an mAb may favor BAR values of 1 or 2. To test this hypothesis, conjugation reactions of BP-Tz to IgG1-TCO and HER2-TCO at feed ratios from 1:1 to 4:1 were conducted (Extended Data Fig. 1). When a 1:1 ratio of BP-Tz to TCO-mAb was used, the major conjugation product had BAR = 1. By contrast, when a 2:1 ratio was used, the mAb was consumed and mostly BAR = 1 or BAR = 2 products formed. Further increasing the reaction stoichiometry gave higher BAR values. Due to size and charge differences between conjugates with zero, one, two or three BPs, we could isolate conjugates with majority BAR = 1, 2 or 3 to study the effects of BAR on antigen binding (Fig. 1f and Supplementary Fig. 6). Dynamic light scattering and cryogenic electron microscopy showed that BP-HER2 conjugates were approximately 25 nm in diameter (Supplementary Fig. 7), which is reasonable given the dimensions of each BP and mAb (approximately 10–15 nm). We note that, although BAR could be controlled using this approach, the exact site of conjugation to the mAb in these cases is not controlled, as lysine conjugation is a stochastic process. To demonstrate that ABC synthesis is compatible with 'site-specific' mAb conjugation techniques, a similar sequence of reactions was carried out using engineered trastuzumab with two reactive cysteine residues (Extended Data Fig. 2 and Supplementary Fig. 8), providing site-specifically modified ABCs with BAR = 1 or BAR = 2.

ABCs show targeting and potency in vitro

We investigated ABC–HER2 binding affinity using microscale thermophoresis (MST) and ELISA assays. Unlike protein conjugates based on flexible linear polymers, which can lead to sterically occluded protein function as molecular weight increases due to folding of the polymer around the biomolecule[49], the rigid backbones of BPs may provide compact structures that extend away from the mAb[50], minimizing impacts on mAb function. PEG-HER2 with BAR = 1 and degrees of polymerization up to 60 displayed solution binding constants by MST that were not significantly different from trastuzumab, TDM-1 (Kadcyla) and T-DXd (Enhertu) (Fig. 1g). Similar trends were observed using ELISA assays (Supplementary Fig. 9), although the ABCs showed moderately lower binding affinities compared to MST, which we attribute to surface occlusion effects inherent to the ELISA assay. Minor reductions in binding affinity and the compact, stable BP architecture could facilitate release of ABCs from perivascular regions of the tumor periphery and facilitate deeper tumor penetration[51,52].

Target-mediated uptake of Cy5.5-HER2 into HER2$^+$ BT-474 and SKBR-3 cells was investigated using flow cytometry (Fig. 1h and Extended Data Figs. 1–3). Conjugates with average BAR ≤ 3 displayed similar levels of SKBR-3 uptake after 1 hour, whereas BAR of 4 showed significantly less cell uptake. Notably, Cy5.5-HER2 was taken up by cells to a more than 100-fold greater extent than non-HER2-targeting variant Cy5.5-IgG1 or Cy5.5-BP alone (Fig. 1h). Cy5.5-HER2 uptake was also increased in SKOV-3 cells, which are HER2$^+$ despite expressing approximately 10-fold less HER2 compared to SKBR-3 (ref. 53) (Extended Data Fig. 4a). Uptakes of Cy5.5-HER2 and Cy5.5-BP were similar in HER2$^-$ MCF-10A cells after different times (10–60 minutes) with varied concentrations (100–250 μg ml^{-1}), confirming the importance of HER2 expression. Confocal fluorescence imaging supported these findings (Fig. 1j), with Cy5.5-HER2 showing substantially greater cell surface binding and uptake compared to Cy5.5-IgG1 and Cy5.5-BP (Extended Data Fig. 3). Furthermore, site-specific cysteine-conjugated Cy5.5-HER2 ABCs exhibited BT-474 cell uptake similar to the lysine-conjugated Cy5.5-HER2 (Extended Data Fig. 2), demonstrating that both conjugation approaches give ABCs capable of efficient cell uptake.

The in vitro cytotoxicities of MMAE-HER2, SN-38-HER2, PTX-HER2 and DOX-HER2 were compared to the analogous BPDs lacking trastuzumab (Fig. 1i and Extended Data Figs. 3 and 4). ABCs were more potent than their corresponding BPDs in HER2$^+$ cell lines SKBR-3, SKOV-3 and BT-474. For example, MMAE-HER2 and MMAE-BPD exhibited IC_{50} values of 7.1 nM and 101.4 nM (Fig. 1i), respectively, after incubation for 24 hours with BT-474 cells. In contrast, ABCs and BPDs displayed similar potencies after incubation for 24 hours and 72 hours with HER2$^-$ MCF-10A cells, which agrees well with their uptake behavior in these cell lines (Fig. 1j and Extended Data Fig. 4). Furthermore, the use of microenvironment mapping (μMap) technology paired with PEG-HER2^{lr} identified the ABC interactome through label-free quantitative proteomic analysis (Fig. 1k and Supplementary Fig. 10)[54]. μMap analysis supports the high-fidelity targeting of the ABC, as HER2 and its interactors (including HER3 and PTK7; typical proteins are highlighted in Fig. 1k) are well preserved (defined by $\log_2$(fold change) > 0.5 and $P < 0.05$) even with the conjugation of the bottlebrush and photocatalyst to trastuzumab.

We note that the ester-based linkers used for these ABCs and BPDs can be cleaved via hydrolysis (Supplementary Fig. 11), akin to the clinical ADC Trodelvy, but their cleavage rates can potentially be accelerated in the presence of hydrolase enzymes present in lysosomal compartments[36,53]; thus, although extracellular hydrolysis likely plays a key role in their potencies, these cytotoxicity results suggest that antigen-mediated cell uptake augments drug release, leading to greater potency within 24 hours than the BPD alone. BPD synthesis is compatible with a wide variety of payload linkers[34–37,55], including peptides that are often used for ADCs[56], suggesting ample room for ABC linker optimization in the future. Notably, it was recently suggested that the efficacy of Enhertu in low-HER2-expressing tumors is due to extracellular drug release, suggesting that both intracellular and extracellular drug release play important roles in the efficacy of targeted drug conjugates[57].

Imaging ABC cell uptake and payload release

The cell uptake and drug release mechanisms of ABCs in BT-474 cells as a function of time were investigated using confocal fluorescence microscopy (Extended Data Fig. 5a). After a short incubation time (10 minutes; Extended Data Fig. 5a, top row), Cy5.5-HER2 was observed to bind to the cell surface. Cell surface binding increased substantially over 4 hours, with ABCs appearing inside the cells (Extended Data Fig. 5a, second row). Most of the ABCs were internalized into endosomal/lysosomal compartments after 24 hours and 72 hours (Extended Data Fig. 5a, third and fourth rows, and Supplementary Fig. 12).

Next, we prepared ABC SN-38-Cy5.5-HER2, which features releasable SN-38 payloads and non-releasable Cy5.5 dyes to enable simultaneous therapy and imaging, respectively. Confocal fluorescence microscopy imaging studies were conducted with this construct, where the intrinsic fluorescence of SN-38 was leveraged to image the payload independently of the Cy5.5-labeled ABC. After 4-hour incubation with SN-38-Cy5.5-HER2, BT-474 cells were washed to remove unbound ABC, and fluorescence signals were collected over time (Extended Data Fig. 5b). After 4 hours, the SN-38 signal overlapped with the Cy5.5 signal, suggesting that the payload is bound to the ABC (Extended Data Fig. 5b,

top row). After 24 hours, the SN-38 signal was still largely co-localized with the ABC signal, but substantial amounts of SN-38 appeared in the cell nuclei separate from the ABC, consistent with the payload being released and transported to the nucleus where SN-38 functions as a topoisomerase I inhibitor (Extended Data Fig. 5b, second row). This separation of SN-38 from the ABC and transport to the nucleus was further enhanced at 72 hours (Extended Data Fig. 5b, third row).

Altogether, these results, combined with µMap results (see above), suggest that ABCs function in a manner that mirrors ADCs (Extended Data Fig. 6). First, ABCs bind to the cell surface through mAb–antigen recognition. Then, bound ABCs are internalized via receptor-mediated endocytosis, and the covalently attached drugs are released through linker (for example, ester) cleavage. Finally, the drugs escape the membrane-encapsulated endosomal/lysosomal vesicles and transport to the relevant intracellular location (for example, the nucleus) where they can exert their intended function based on their MoA. As noted above, cell-surface-bound or unbound ABCs likely also release payload extracellularly in the tumor microenvironment, which can contribute to the 'bystander effect' and improve efficacy in low-antigen-expressing tumors[57]. Extracellular, particularly systemic, release could increase the risk of off-target toxicity, which can be mitigated in the future by designing cleavable linkers that respond more selectively to triggers within the tumor microenvironment[4,22,56]. Overall, the mechanistic information presented in Extended Data Fig. 5 is observable due to the versatility of ABC synthesis, where both Cy5.5 and SN-38 were incorporated into one BPD via co-polymerization. In the future, this strategy can be used to enable mAb-targeted combination therapies wherein a single ABC could carry a defined number and ratio of multiple payloads.

ABCs show long half-lives and tumor accumulation

Encouraged by the in vitro cell culture results described above, we considered other aspects of ABC function that will become important for their further translation. For example, interactions between the mAb Fc domain and the neonatal fragment crystallizable receptor (FcRn) play an important role in enhancing the circulation half-life of mAbs and ADCs[58]. FcRn binding assays (Fig. 2a) suggested that ABCs preserve this function, with affinities similar to unmodified trastuzumab and other HER2-targeted ADCs. Next, we assessed the blood pharmacokinetics of Cy5.5-HER2, Cy5.5-IgG1, Cy5.5-BP and Cy5.5-labeled trastuzumab (Cy5.5-TmAb) in NCR nude mice after tail vein injection; more than 40% injected dose of each ABC and BPD construct was present in circulation after 24 hours (Fig. 2b), and more than 30% remained after 3 days (Fig. 2b,c). By contrast, Cy5.5-TmAb was not detectable in blood after 3 days (Fig. 2c). Ex vivo tissue biodistribution was assessed as a function of time after tail vein injection into NCR nude mice bearing subcutaneous BT-474 tumors (80 ± 10 mm^3). Although Cy5.5-HER2, Cy5.5-IgG1 and Cy5.5-BP displayed similar biodistribution within 12 hours (Extended Data Fig. 7), the HER2-targeted ABC Cy5.5-HER2 showed substantially greater tumor accumulation over the course of 36 hours and 72 hours compared to the non-targeted controls (Fig. 2d–f). By contrast, Cy5.5-TmAb displayed significant accumulation in the liver (Supplementary Fig. 13). These results suggest that the extended circulation and tumor targeting of ABCs may confer beneficial therapeutic effects in vivo. Moreover, they highlight how direct conjugation of hydrophobic molecules to mAbs—for example, Cy5.5-TmAb—can disrupt mAb function, whereas shifting the hydrophobic payloads to BPs can preserve mAb function.

ABCs show in vivo efficacy across broad drug potencies

Next, we turned to investigating the efficacy and safety of ABCs with various drugs in murine tumor models. MMAE is one of the most widely used drugs for clinical ADCs[59]; thus, to assess whether ABCs could function in vivo, we began our studies using MMAE-based ABCs as a model system. Notably, MMAE-HER2 was much more potent than MMAE-BP toward $HER2^+$ BT-474 cells in vitro (Extended Data Fig. 8a). Thus, we examined ABCs MMAE-HER2 (DAR = 135; BAR = 3), MMAE-IgG1 (DAR = 135; BAR = 3; non-HER2-targeted ABC) and MMAE-BP (BPD only) and saline controls in vivo using a BT-474 mouse xenograft model. Each construct was administered via tail vein injection into mice ($n = 4$ per group) bearing subcutaneous BT-474 tumors once weekly for 4 weeks (5 mg kg^{-1} mAb or 1.7 mg kg^{-1} MMAE per dose). This antibody dose was selected for consistency with reported preclinical ADC efficacy studies and following common clinical dosing of ADCs (approximately 1–10 mg kg^{-1})[30,60]. The tumors in the control group grew continuously over the course of 40 days (Fig. 3a and Extended Data Fig. 8b), and the non-targeted controls MMAE-IgG1 and MMAE-BP significantly retarded tumor growth, presumably via passive tumor accumulation through the enhanced permeability and retention effect[61]. MMAE-HER2 displayed superior tumor regression as determined by tumor volume, ex vivo tumor weight and histopathologic evaluation of the xenograft site where no tumor cells were visible (Fig. 3c and Extended Data Figs. 8c and 9). Body weight measurements suggested that all the constructs were well tolerated at the doses given (Fig. 3b). Moreover, histopathologic evaluation of major organs (heart, lung, liver, spleen and kidney) revealed no signs of toxicity (Extended Data Fig. 9).

Although the above study was encouraging, the ultra-high DAR of MMAE-HER2 leads to a drug dose that is substantially greater than the doses of MMAE in ADCs given to patients in the clinic. Thus, we sought to investigate less potent payloads, which would potentially benefit more from the ultra-high DAR of these ABCs while maintaining clinically relevant drug doses. Similar studies were conducted using SN-38-HER2. SN-38 is given in prodrug form (irinotecan) in the clinic, it is the payload in the clinical ADC sacituzumab govitecan (Trodelvy)[27,28] and it represents a much broader class of popular topoisomerase I inhibitor ADC payloads, including DXd. For comparison in vitro, we also prepared an ADC, SN-38-ADC, with SN-38 (DAR = 2.5) and trastuzumab as the targeting moiety, using a similar ester linker. In vitro cytotoxicity studies showed that the ABC HER2-SN-38 exhibits significantly higher potency when normalized to the antibody concentration (Supplementary Fig. 14), as expected due to the larger drug dose. Then, mice ($n = 6$) bearing BT-474 tumors were given SN-38-HER2 and the non-targeted analogs SN-38-IgG1 and SN-38-BP (5 mg kg^{-1} mAb; 1.1 mg kg^{-1} SN-38) via tail vein injection twice weekly for seven total doses. SN-38-HER2 displayed superior tumor regression (Fig. 3d and Extended Data Fig. 8d) and led to 100% survival (Fig. 3f) after 280 days. In contrast, the mice in the control and non-trastuzumab groups displayed substantial tumor growth (Fig. 3d) and similarly poor survival outcomes (Fig. 3f). The constructs were well tolerated as determined by body weight measurements (Fig. 3e). Notably, the drug doses used here are similar to those used clinically for SN-38 prodrugs such as irinotecan.

Encouraged by these studies, we next investigated ABCs with doxorubicin (DOX) as the payload. DOX is a topoisomerase II poison used clinically in liposomal and free drug forms for various solid and liquid cancers; its low potency (approximately 10-fold less than SN-38 and approximately 100-fold less than MMAE) makes it a poor candidate for traditional ADCs, and attempts to use it in this context failed[10,62]. For example, the DOX-based ADC BR-96 was given at very high doses of 700 mg m^{-2} (approximately 17.3 mg kg^{-1}) of mAb in the clinic[62]. Such high doses can potentially lead to diminishing therapeutic returns[63] and a narrow therapeutic window. To maintain the 1–10 mg kg^{-1} mAb dose used for ADCs in the clinic today while also enabling much less potent payloads such as DOX, a higher DAR could be advantageous (Supplementary Fig. 15). BT-474 tumor-bearing mice ($n = 6$) given DOX-HER2 (5 mg kg^{-1} mAb; 1.9 mg kg^{-1} DOX) once per week for 4 weeks showed no visible tumor at the xenograft site (Fig. 3g,i and Extended Data Fig. 8e–g); non-targeted DOX-IgG1 and DOX-BP showed no efficacy at the same doses. Here again, the constructs were well-tolerated (Fig. 3h) at the doses given, which are similar to the clinical doses of free DOX.

https://doi.org/10.1038/s41587-025-02772-z

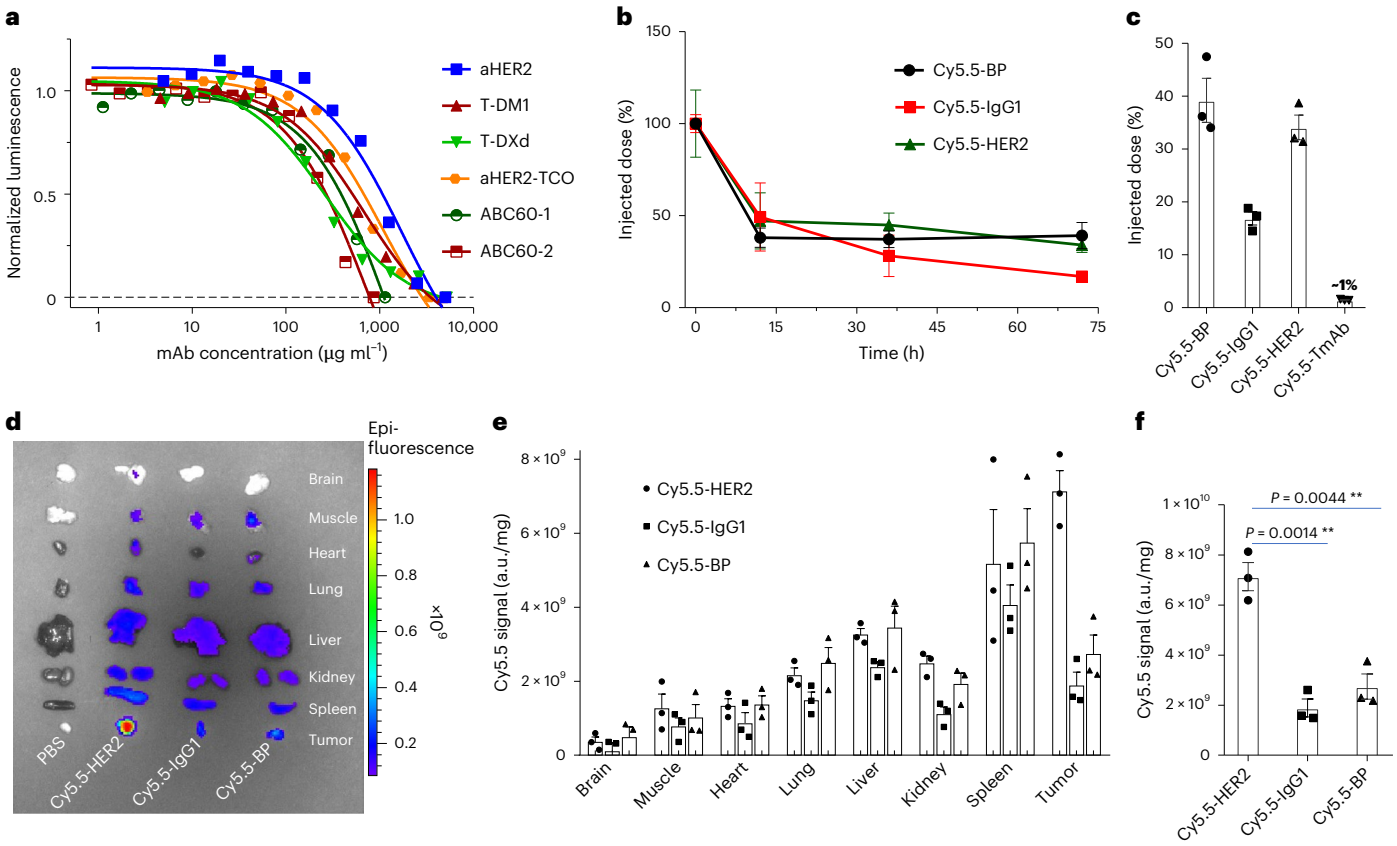

Fig. 2 | Pharmacokinetics and biodistribution of ABCs. a, FcRn binding assay comparing HER2-targeted ABCs to trastuzumab (aHER2) and ADCs T-DM1 and T-DXd. ABC60-1 refers to an ABC with DAR = 60 and BAR = 1. ABC60-2 refers to an ABC with DAR = 60 and BAR = 2. **b**, Blood PK studies comparing BPD Cy5.5-BP, non-HER2-targeted Cy5.5-IgG1 and Cy5.5-HER2 as assessed by fluorescence imaging of blood samples ($n = 3$ biological replicates). **c**, Total percentage of injected dose in blood 72 hours after injection of each construct, as assessed by fluorescence imaging ($n = 3$ biological replicates). **d**, Ex vivo images of different organs and tumors of mice bearing subcutaneous BT-474 tumors 72 hours after administration of each construct. Only HER2-targeted Cy5.5-HER2 shows selective tumor accumulation over this timescale. **e**, Quantitative BD results obtained via fluorescence quantification 72 hours after administration to mice bearing subcutaneous BT-474 tumors ($n = 3$ biological replicates). **f**, Zoomed-in BD results for tumor tissue fluorescence signal 72 hours after injection. Results are presented as mean ± s.e.m. ($n = 3$ biological replicates). Statistical analysis was done using a two-tailed t-test. For these statistical tests, '**' denotes $P < 0.01$. BD, biodistribution; PK, pharmacokinetics.

Efficacy comparison between ABCs and clinical ADCs

Having shown that HER2-targeting ABCs outperform their non-targeting IgG1-based ABCs and BPD counterparts, we proceeded to benchmark them against commercially available ADCs[47]. First, we compared the single-dose efficacy of ABCs MMAE-HER2, SN-38-HER2, DOX-HER2 and PEG-HER2 (that is, no payload) to Kadcyla (T-DM1; payload: mertansine (DM1); DAR = 3.8) at the same antibody dose (5 mg kg^{-1}) using the BT-474 model described above. Although PEG-HER2 displayed some efficacy, presumably due to HER2 antagonism analogous to Herceptin, each payload-containing ABC and T-DM1 performed much better (Fig. 4a). Tumor volume comparisons after 40 days revealed that, although the ABCs displayed a clear efficacy–payload potency trend, all three ABCs exhibited superior efficacy compared to Kadcyla (Fig. 4b,c); ex vivo images (Fig. 4d) and tumor mass (Figs. 4e,f) measurements generally supported these results. We attribute the performance of DOX-HER2, which has a much less potent (approximately 100×) payload compared to Kadcyla, to its high DAR, which allows administering the same mAb dose while achieving an effective payload dose.

Encouraged by these findings, we next compared an SN-38-HER2 ABC (BAR = 1; DAR = 60; this construct was selected to further lower the dose of SN-38 compared to the study described above) and the ADC T-DXd (payload: DXd; DAR = 7.7), a biosimilar of the drug Enhertu that also uses a topoisomerase I inhibitor payload (DXd). In the high HER2$^+$ BT-474 tumor model with initial tumor sizes of approximately 200 mm^3, both constructs displayed efficacy (Fig. 4g); however, in an orthotopic tumor model with very low HER2 expression (HCC-70 (ref. 64); 5 mg kg^{-1} antibody for each construct given every 10 days for three total doses), SN-38-HER2 displayed superior efficacy compared to T-DXd (Fig. 4h). We attribute this performance to the ultra-high DAR of SN-38-HER2, which delivers a greater number of topoisomerase I inhibitor drug molecules to the tumor after either antigen-mediated uptake or extracellular release[57] when given at the same mAb dose. Here again, all the constructs were well tolerated at the doses given (Supplementary Fig. 16), which are again within the range of clinical doses of SN-38 prodrugs.

ABCs enable targeted protein degradation using a proteolysis-targeting chimera

Given the therapeutic efficacy demonstrated by ABCs with payloads from a diverse range of drugs that are used in clinical ADCs (MMAE and SN-38) or given as free drugs in the clinic (DOX), we set out to apply ABCs for the targeted delivery of a potential next-generation payload class: proteolysis-targeting chimeras (PROTACs)[65–68]. Although PROTACs have garnered a great deal of attention in recent years, their physical properties and pharmacokinetic limitations have necessitated the use of frequent, high doses (for example, daily doses of 10–100 mg kg^{-1}) to achieve in vivo efficacy in murine models[69–72] and have posed substantial translational challenges[65–68]. Antibody conjugation (for example,

https://doi.org/10.1038/s41587-025-02772-z

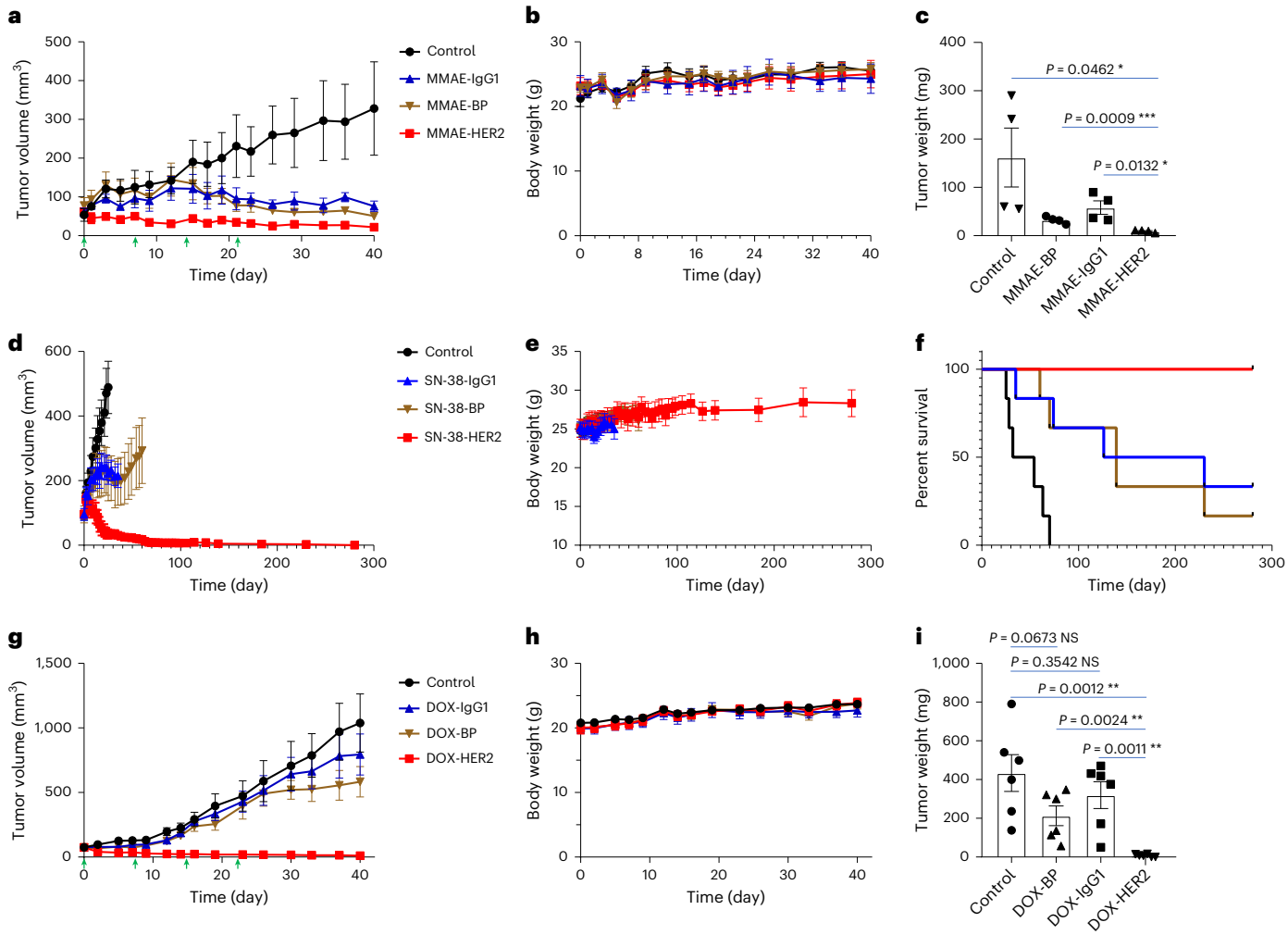

Fig. 3 | Efficacy and safety of ABCs incorporating diverse payloads with different potencies in HER2$^+$ BT-474 tumor-bearing mice. Tumor volumes versus time (**a**), body weights versus time (**b**) and tumor weight measurements after 40 days (**c**) for mice given MMAE-based constructs (5 mg kg^{-1} mAb or 1.7 mg kg^{-1} MMAE per dose). Mice were dosed once a week for a total of four doses as illustrated via green arrows in **a** ($n = 4$ mice per group). Tumor volumes versus time (**d**), body weights versus time (**e**) and survival curves (**f**) for mice given SN-38-based constructs (5 mg kg^{-1} mAb or 1.1 mg kg^{-1} SN-38 per dose). Mice were dosed twice a week with a total of seven doses (dose schedule is illustrated in Extended Data Fig. 8d) ($n = 6$ mice per group). Tumor volumes versus time (**g**), body weights versus time (**h**) and tumor weight measurements after 40 days (**i**) for mice given DOX-based constructs (5 mg kg^{-1} mAb or 1.9 mg kg^{-1} DOX per dose). Mice were dosed once per week for a total of four doses as illustrated by the green arrows in **g** ($n = 6$ mice per group). Results are presented as mean ± s.e.m. Statistical analysis was done using a two-tailed t-test. For these statistical tests, NS denotes non-significant; $^*P < 0.05$; $^{**}P < 0.01$.

PROTAC-based ADCs) could potentially overcome these challenges by imparting improved pharmacokinetics and enhancing target cell uptake[73]. Here, we selected ARV771 to test this idea, as it is one of the most extensively studied PROTACs, degrading bromodomain and extra-terminal (BET) motif proteins responsible for regulating gene expression, ultimately leading to cell death. The Von Hippel–Lindau (VHL) protein binding moiety of ARV771 features a hydroxyl group conducive to facile linker conjugation. Thus, following the same general strategy outlined above, we prepared ABC ARV771-HER2 (DAR = 135; BAR = 3; Supplementary Fig. 17a) and its non-targeted analogs ARV771-IgG1 and ARV771-BP. ARV771-HER2 displayed greater potency in vitro after 48-hour incubation compared to its non-targeted ARV771-BP (Supplementary Fig. 17b), and its MoA of BRD4 degradation was confirmed, although higher doses of ABC compared to ARV771 were needed to achieve similar BRD4 degradation in vitro due to the slow release of ARV771 from the ABC (Supplementary Fig. 17c). We then compared the efficacy of ARV771-HER2 to its non-targeted counterparts, ARV771 alone and a related PROTAC, ARV825, that leverages cereblon rather than VHL to achieve BRD4 degradation, using the BT-474 tumor model (Fig. 5a). Each construct was given via tail vein injection once weekly for 3 weeks (5 mg kg^{-1} mAb; 3 mg kg^{-1} ARV771), and all were well tolerated at this dose (Fig. 5b); however, only ABC ARV771-HER2 displayed efficacy in this model at this dose (Fig. 5a,c), leading to nearly complete disappearance of the tumor at the xenograft site (Fig. 5d,e), whereas the non-targeted constructs displayed no substantial efficacy. These results suggest that ABCs could facilitate infrequent, low dosing of PROTACs to substantially improve their efficacy in vivo.

ABCs are compatible with other mAbs for targeting

Finally, we sought to demonstrate the modularity and scope of ABCs beyond HER2 targeting. MUC1 was selected as a potential target. MUC1 is overexpressed in diverse cancer types, including ovarian, lung and breast cancers[74], and it currently ranks as the second most promising antigen among 75 candidates according to the National Cancer Institute[75]. Here, Cy5.5-BP, MMAE-BP and PTX-BP were conjugated to a TCO-functionalized anti-MUC1 mAb following the same protocols used above for trastuzumab conjugation to BPDs, giving MUC1-targeted ABCs Cy5.5-MUC1, MMAE-MUC1 and PTX-MUC1 (DAR ≈ 135; BAR ≈ 3;

https://doi.org/10.1038/s41587-025-02772-z

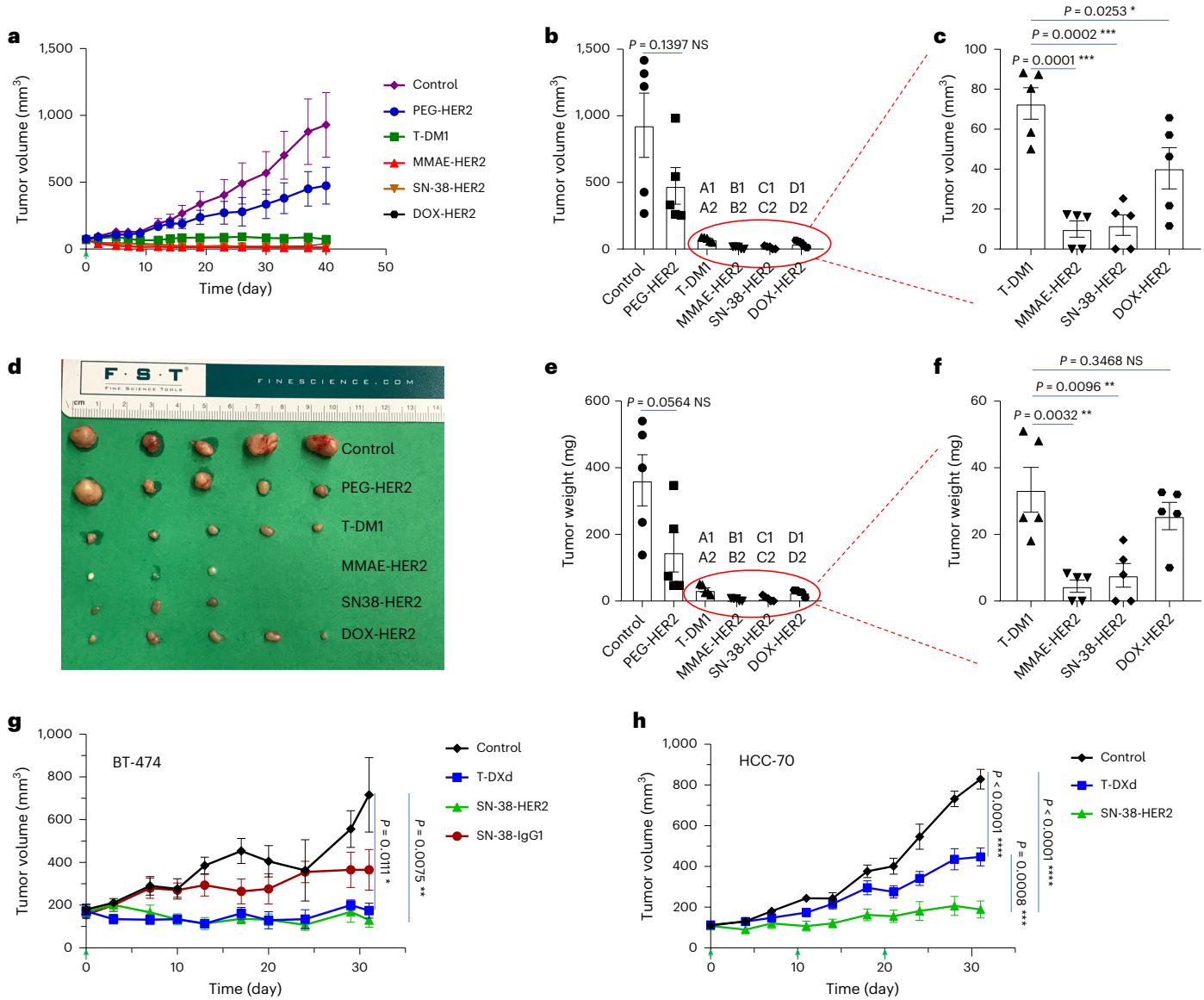

Fig. 4 | Efficacy of HER2-targeted ABCs with different payloads and commercial HER2-targeted ADCs T-DM1 and T-DXd in high and low HER2 tumors. a, Tumor volumes versus time for MMAE, SN-38 and DOX-based ABCs compared to T-DM1 and a non-payload-containing PEG bottlebrush–trastuzumab conjugate, PEG-HER2, in HER2$^+$ subcutaneous BT-474 tumor-bearing mice. When tumor volumes reached approximately 100 mm^3, mice were randomized into treatment and control groups (5 mg kg^{-1} mAb per dose; mice were dosed on day 0 as illustrated by the green arrow on the *x* axis; $n = 5$ mice per group). **b**, Tumor volumes after 40 days for all groups. A1, B1, C1 and D1 are the statistical analyses with the control group; A1: $P = 0.0075$ (**), B1: $P = 0.0052$ (**), C1: $P = 0.0052$ (**), D1: $P = 0.0062$ (**). A2, B2, C2 and D2 are the statistical analyses with the PEG-HER2 group; A2: $P = 0.0194$ (*), B2: $P = 0.0097$ (**), C2: $P = 0.0099$ (**), D2: $P = 0.0137$ (*). **c**, Zoomed-in view of tumor volumes for payload-containing ABCs and T-DM1, showing that ABCs display payload-potency-dependent efficacy and improved efficacy for all payloads compared to T-DM1. **d**, Ex vivo image of tumors from each group at day 40. **e**, Tumor weight measurement after 40 days for all groups. A1, B1, C1 and D1 are the statistical analyses with the control group; A1: $P = 0.0027$ (**), B1: $P = 0.0016$ (**), C1: $P = 0.0017$ (**), D1: $P = 0.0023$ (**). A2, B2, C2 and D2 are the statistical analyses with the PEG-HER2 group; A2: $P = 0.094$ (NS), B2: $P = 0.0432$ (*), C2: $P = 0.0473$ (*), D2: $P = 0.0757$ (NS). **f**, Zoomed-in view of tumor volumes for payload-containing ABCs and T-DM1, showing that ABCs display payload-potency-dependent efficacy and improved efficacy for all payloads compared to T-DM1. **g**, Tumor volumes versus times for BT-474 tumor-bearing mice after a single dose of SN-38-HER2, non-targeted SN-38-IgG1 or T-DXd. Once tumor volumes reached approximately 175 mm^3, mice were randomized into treatment and control groups. Mice were given a single dose (5 mg kg^{-1} mAb) of each construct intravenously at day 0 ($n = 5$ mice per group; control group: $n = 4$). **h**, Tumor volumes versus times for NCR nude mice bearing orthotopic, low-HER2-expressing HCC-70 tumors after injection of SN-38-HER2 or T-DXd ($n = 8$ mice per group). At tumor volumes of approximately 100 mm^3, mice were randomized into treatment and control groups. Mice were administered each construct intravenously once every 10 days for three total doses as indicated by the green arrows. Results are presented as mean ± s.e.m. Statistical analysis was done using a two-tailed *t*-test. For these statistical tests, NS denotes non-significant; *$P < 0.05$; **$P < 0.01$; ***$P < 0.001$.

Supplementary Fig. 18a). Cy5.5-MUC1 exhibited approximately 100× improved cell engagement (MUC1$^+$ CAOV-3 ovarian cancer cells) by flow cytometry compared to non-targeted controls (Supplementary Fig. 18b), whereas PTX-MUC1 and MMAE-MUC1 displayed greater potency in vitro after 48-hour incubation compared to non-targeted controls (Supplementary Fig. 18c,d). Moreover, Cy5.5-MUC1 displayed greater CAOV-3 tumor accumulation in vivo as determined by ex vivo imaging (Fig. 6a).

Encouraged by these results, we studied the efficacy of MMAE-MUC1 in NCR nude mice bearing subcutaneous CAOV-3 tumors (3.75 mg kg^{-1} mAb; 1.28 mg kg^{-1} payload; given every 7 days for four total doses). Like the findings shown above for HER2-targeted ABCs, MMAE-MUC1 substantially outperformed its non-targeted counterparts, leading to no visible tumor at the xenograft site over 60 days while being well tolerated (Fig. 6b–f).

https://doi.org/10.1038/s41587-025-02772-z

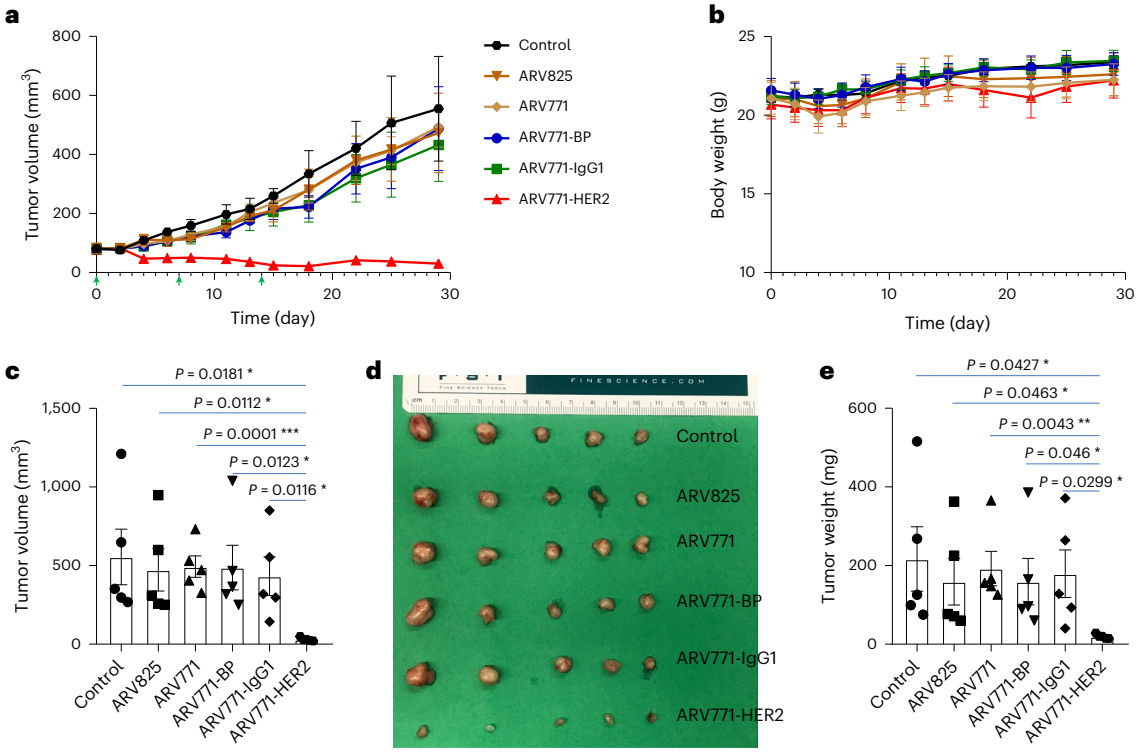

Fig. 5 | Efficacy and safety of ABCs incorporating the PROTAC payload ARV771 in HER2$^+$ BT-474 tumor-bearing mice. Tumor volumes versus time (**a**), body weights versus time (**b**), tumor volumes at day 30 (**c**), ex vivo images of tumors at day 30 (**d**) and tumor weight measurements at day 30 (**e**) for mice bearing subcutaneous BT-474 tumors. Once tumors reached approximately 100 mm^3, mice were randomized into treatment and control groups. Mice were given each PROTAC construct intravenously once per week for three total doses, as indicated by the green arrows in **a** ($n = 5$ mice per group). Note that two PROTACs were tested as free drugs, ARV771 and ARV825, for comparison to ABC ARV771-HER2. At the doses given, the free PROTACs and non-targeted controls are not effective, whereas ARV771-HER2 leads to near tumor eradication. Results are presented as mean ± s.e.m. Statistical analysis was done using a two-tailed *t*-test. For these statistical tests, NS denotes non-significant; $^*P < 0.05$.

Discussion

We present ABCs that enable the modular synthesis of targeted cancer therapeutics. ABCs are synthesized through a BPD termination reaction that installs one 'click' chemistry functional handle onto the BPD chain end; subsequent bioconjugation using either stochastic or site-specific reactions provides a convenient strategy to generate ABCs with different drug compositions and targeting agents, as demonstrated herein using multiple payloads and two different targeting mAbs. ABCs show efficacy in vivo with traditional ADC payloads (for example, MMAE and SN-38) and drugs with MoAs that have not yet been successfully used in clinical ADCs (for example, DOX and ARV771). ABC synthesis facilitates rapid, consistent manufacturing, as demonstrated here for different drugs, combinations of drugs and imaging agents (for example, SN-38 and Cy5.5) and antigen targets (HER2 and MUC1). Moreover, selected ABCs display superior efficacy in murine models compared to clinical ADCs with no observable toxicities. Given the modularity of ABC manufacturing, we expect that it will be possible to extend these concepts to payload combinations and alternative targeting agents, such as small molecules, peptides or even cells, in the future[76].

Because ABCs move the payloads from the antibody surface onto the backbone of the BPDs, they introduce several features compared to standard ADCs, but they also raise questions. For example, in contrast to ADCs, which are limited to DARs of approximately 8 due to the inherent functionality of mAbs, ABCs can achieve 1–2 orders of magnitude greater DAR values. Traditionally, higher DARs can lead to deterioration of ADC physical properties, and, as a result, having a higher DAR does not necessarily translate to improved ADC function[77]. ABCs allow for access to ultra-high DARs with potentially reduced impacts on physical properties, thereby opening access to regimes of payload diversity for targeted therapeutics. For example, we propose that for low-potency payloads—that is, payloads that are approximately 10–100-fold less potent than current ADC payloads, which represent the majority of small-molecule anticancer drugs—increasing DAR may be the only way to practically utilize such payloads by compensating for their lower per-payload potency. Thus, being able to access ultra-high DAR values could facilitate the use of a broader landscape of drugs in the ABC context, including payloads with improved therapeutic windows imparted by their MoA. In the future, combining mAb-based surface antigen targeting, which creates a therapeutic window through cell-selective delivery, with MoA-driven payload targeting, where the therapeutic window is generated through targeting of biological pathways that drive disease, may enable more effective and safer cancer therapies by leveraging both biological and pharmacological selectivity. Nevertheless, these potential benefits of ABCs raise questions, such as how the BPD will potentially impact the safety, biodistribution and pharmacokinetic properties of ABCs compared to ADCs and other delivery systems as they progress toward clinical applications. BPDs are designed to achieve tunable, high DARs while staying as compact as possible and by presenting PEG sidechains that may confer pharmacokinetic and safety advantages. Moreover, BPs have been shown to display advantageous pharmacokinetic and tissue penetration properties when compared to spherical or linear counterparts of similar molecular weight[78–80]. Nevertheless, ABCs are larger than ADCs, which may alter their pharmacokinetics and biodistribution. If necessary, smaller PEG sidechains can be used to further compress the BPD size, although, at some point, the beneficial 'shielding' of the payload and linker sidechains may be compromised if these sidechains are too short. Other translational questions, such as

https://doi.org/10.1038/s41587-025-02772-z

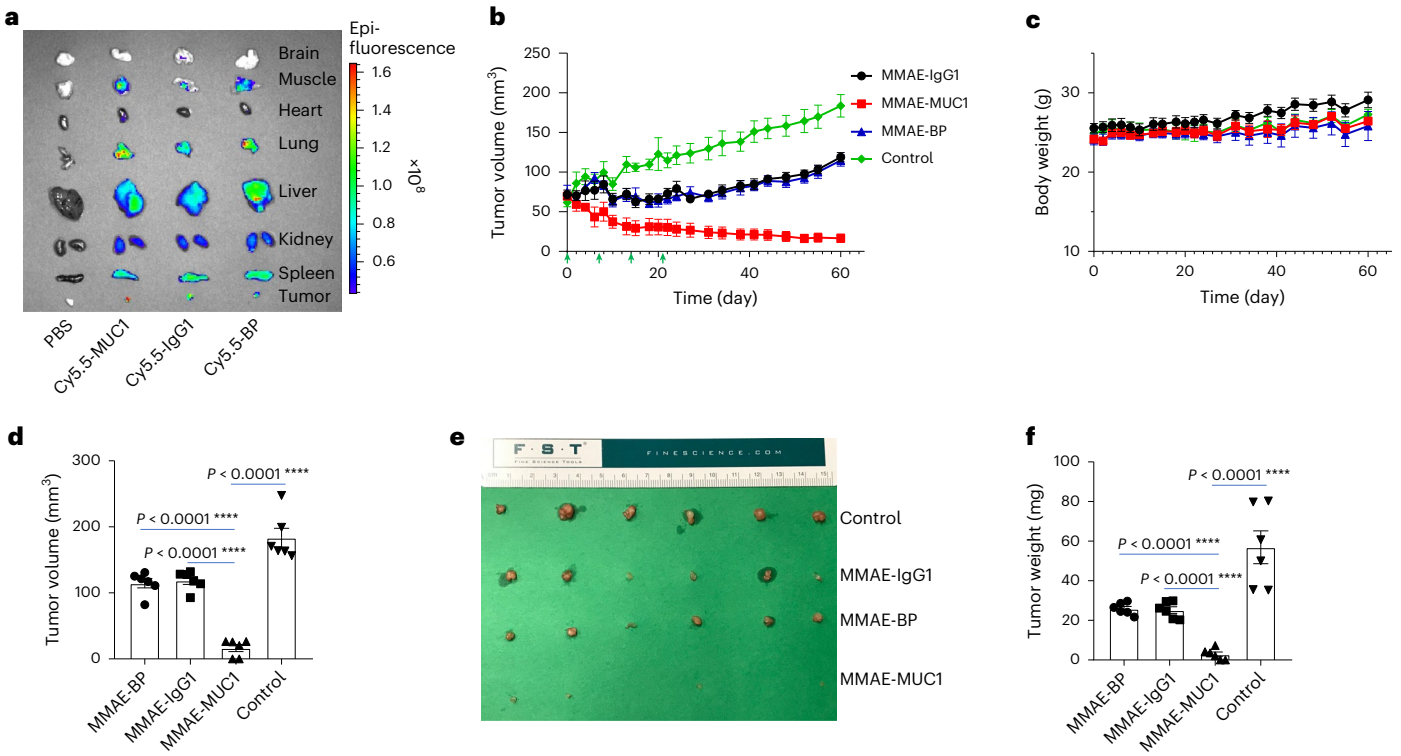

Fig. 6 | Biodistribution, efficacy and safety of MUC1-targeted ABCs in ovarian cancer (CAOV-3) tumor-bearing mice. a, Ex vivo biodistribution 72 hours after administration showing increased fluorescence in tumors of mice given MUC1-targeted Cy5.5-MUC1. Tumor volumes versus time (**b**), body weights versus time (**c**), tumor volumes at day 60 (**d**), ex vivo images of tumors at day 60 (**e**) and tumor weights at day 60 (**f**) for NCR nude mice bearing subcutaneous CAOV-3 tumors ($n = 6$ mice per group). At tumor volumes of approximately 80 mm^3, mice were randomized into treatment and control groups. Mice were given each construct intravenously once per week for four total doses as indicated by the green arrows in **b**. Results are presented as mean ± s.e.m. ($n = 6$ mice per group). Statistical analysis was done using a two-tailed *t*-test. For these statistical tests, '****' denotes $P < 0.0001$.

long-term clearance and immunogenicity of ABCs, must be examined, although we are encouraged by the fact that PEGylated therapeutics are widely used in the clinic, and BPs and BPDs have been shown to be safe and non-immunogenic in various preclinical assays[81]. Moreover, the PEG chains of BPDs can be exchanged for other hydrophilic, non-immunogenic components, such as polyoxazolines[82], and backbone degradability to facilitate tissue clearance can be built into BPD constructs through simple co-polymerization reactions[83]; investigating the impacts of such compositional changes on ABC function will guide the future of ABC design. Additionally, questions related to payload–linker release deserve further detailed investigation in the future. In the present study, we leveraged ester-based functional groups as cleavable linkers in ABCs, which function through a combination of hydrolysis and potential accelerated cleavage upon cell uptake. Although such linkers are viable for ADC development, as demonstrated with Trodelvy, most clinical ADCs utilize peptide-based linkers that display improved serum stability. Although it is straightforward to incorporate peptide-based linkers into BPDs as well[56], their impact on ABC function and comparison to the ester-based linkers reported here have not yet been investigated; identifying combinations of linkers and payloads that combine good serum stability with rapid release upon cell uptake will be a continued avenue of investigation.

Online content

Any methods, additional references, Nature Portfolio reporting summaries, source data, extended data, supplementary information, acknowledgements, peer review information; details of author contributions and competing interests; and statements of data and code availability are available at https://doi.org/10.1038/s41587-025-02772-z.

References

1. Siegel, R. L., Miller, K. D., Fuchs, H. E. & Jemal, A. Cancer statistics, 2022. *CA Cancer J. Clin.* **72**, 7–33 (2022).
2. Wang, Z., Li, H., Gou, L., Li, W. & Wang, Y. Antibody–drug conjugates: recent advances in payloads. *Acta Pharm. Sin. B* **13**, 4025–4059 (2023).
3. Hobson, A. D. Chapter One - Antibody drug conjugates beyond cytotoxic payloads. *Prog. Med. Chem.* **62**, 1–59 (2023).
4. Tarantino, P., Ricciuti, B., Pradhan, S. M. & Tolaney, S. M. Optimizing the safety of antibody–drug conjugates for patients with solid tumours. *Nat. Rev. Clin. Oncol.* **20**, 558–576 (2023).
5. Dumontet, C., Reichert, J. M., Senter, P. D., Lambert, J. M. & Beck, A. Antibody–drug conjugates come of age in oncology. *Nat. Rev. Drug Discov.* **22**, 641–661 (2023).
6. Chalouni, C. & Doll, S. Fate of antibody-drug conjugates in cancer cells. *J. Exp. Clin. Cancer Res.* **37**, 20 (2018).
7. Tashima, T. Delivery of drugs into cancer cells using antibody–drug conjugates based on receptor-mediated endocytosis and the enhanced permeability and retention effect. *Antibodies* **11**, 78 (2022).
8. ADCs' revival. *Nat. Biotechnol.* **41**, 740 (2023).
9. Tarantino, P. et al. Antibody–drug conjugates: smart chemotherapy delivery across tumor histologies. *CA Cancer J. Clin.* **72**, 165–182 (2022).
10. Beck, A., Goetsch, L., Dumontet, C. & Corvaïa, N. Strategies and challenges for the next generation of antibody–drug conjugates. *Nat. Rev. Drug Discov.* **16**, 315–337 (2017).
11. Drago, J. Z., Modi, S. & Chandarlapaty, S. Unlocking the potential of antibody–drug conjugates for cancer therapy. *Nat. Rev. Clin. Oncol.* **18**, 327–344 (2021).

12. Gan, H. K., van den Bent, M., Lassman, A. B., Reardon, D. A. & Scott, A. M. Antibody–drug conjugates in glioblastoma therapy: the right drugs to the right cells. *Nat. Rev. Clin. Oncol.* **14**, 695–707 (2017).
13. Fu, Z., Li, S., Han, S., Shi, C. & Zhang, Y. Antibody drug conjugate: the 'biological missile' for targeted cancer therapy. *Signal Transduct. Target. Ther.* **7**, 93 (2022).
14. Tong, J. T. W., Harris, P. W. R., Brimble, M. A. & Kavianinia, I. An insight into FDA approved antibody-drug conjugates for cancer therapy. *Molecules* **26**, 5847 (2021).
15. Criscitiello, C., Morganti, S. & Curigliano, G. Antibody–drug conjugates in solid tumors: a look into novel targets. *J. Hematol. Oncol.* **14**, 20 (2021).
16. Nagayama, A., Ellisen, L. W., Chabner, B. & Bardia, A. Antibody–drug conjugates for the treatment of solid tumors: clinical experience and latest developments. *Target. Oncol.* **12**, 719–739 (2017).
17. Jabbour, E., Paul, S. & Kantarjian, H. The clinical development of antibody–drug conjugates—lessons from leukaemia. *Nat. Rev. Clin. Oncol.* **18**, 418–433 (2021).
18. Yu, B. & Liu, D. Antibody-drug conjugates in clinical trials for lymphoid malignancies and multiple myeloma. *J. Hematol. Oncol.* **12**, 94 (2019).
19. Zhao, P. et al. Recent advances of antibody drug conjugates for clinical applications. *Acta Pharm. Sin. B* **10**, 1589–1600 (2020).
20. Nessler, I., Menezes, B. & Thurber, G. M. Key metrics to expanding the pipeline of successful antibody–drug conjugates. *Trends Pharmacol. Sci.* **42**, 803–812 (2021).
21. Mckertish, C. M. & Kayser, V. Advances and limitations of antibody drug conjugates for cancer. *Biomedicines* **9**, 872 (2021).
22. Su, Z. et al. Antibody–drug conjugates: recent advances in linker chemistry. *Acta Pharm. Sin. B* **11**, 3889–3907 (2021).
23. Abelman, R. O., Wu, B., Spring, L. M., Ellisen, L. W. & Bardia, A. Mechanisms of resistance to antibody–drug conjugates. *Cancers* **15**, 1278 (2023).
24. Nguyen, T. D., Bordeau, B. M. & Balthasar, J. P. Mechanisms of ADC toxicity and strategies to increase ADC tolerability. *Cancers* **15**, 713 (2023).
25. Chudasama, V., Maruani, A. & Caddick, S. Recent advances in the construction of antibody–drug conjugates. *Nat. Chem.* **8**, 114–119 (2016).
26. Lyon, R. P. et al. Reducing hydrophobicity of homogeneous antibody-drug conjugates improves pharmacokinetics and therapeutic index. *Nat. Biotechnol.* **33**, 733–735 (2015).
27. Adams, E., Wildiers, H., Neven, P. & Punie, K. Sacituzumab govitecan and trastuzumab deruxtecan: two new antibody–drug conjugates in the breast cancer treatment landscape. *ESMO Open* **6**, 100204 (2021).
28. Goldenberg, D. M. & Sharkey, R. M. Sacituzumab govitecan, a novel, third-generation, antibody-drug conjugate (ADC) for cancer therapy. *Expert Opin. Biol. Ther.* **20**, 871–885 (2020).
29. Modi, S. et al. Trastuzumab deruxtecan in previously treated HER2-positive breast cancer. *N. Engl. J. Med.* **382**, 610–621 (2020).
30. Rubahamya, B., Dong, S. & Thurber, G. M. Clinical translation of antibody drug conjugate dosing in solid tumors from preclinical mouse data. *Sci. Adv.* **10**, eadk1894 (2024).
31. Kukkar, D., Kukkar, P., Kumar, V., Hong, J. & Kim, K. H. A. Deep, recent advances in nanoscale materials for antibody-based cancer theranostics. *Biosens. Bioelectron.* **173**, 112787 (2021).
32. Yurkovetskiy, A. V. et al. Dolaflexin: a novel antibody–drug conjugate platform featuring high drug loading and a controlled bystander effect. *Mol. Cancer Ther.* **20**, 885–895 (2021).
33. Müllner, M. Molecular polymer bottlebrushes in nanomedicine: therapeutic and diagnostic applications. *Chem. Commun.* **58**, 5683–5716 (2022).
34. Johnson, J. A. et al. Core-clickable PEG-*branch*-azide bivalent-bottle-brush polymers by ROMP: grafting-through and clicking-to. *J. Am. Chem. Soc.* **133**, 559–566 (2011).
35. Golder, M. R. et al. Reduction of liver fibrosis by rationally designed macromolecular telmisartan prodrugs. *Nat. Biomed. Eng.* **2**, 822–830 (2018).
36. Bhagchandani, S. H. et al. Engineering kinetics of TLR7/8 agonist release from bottlebrush prodrugs enables tumor-focused immune stimulation. *Sci. Adv.* **9**, eadg2239 (2023).
37. Liao, L. et al. A convergent synthetic platform for single-nanoparticle combination cancer therapy: ratiometric loading and controlled release of cisplatin, doxorubicin, and camptothecin. *J. Am. Chem. Soc.* **136**, 5896–5899 (2014).
38. Kolb, H. C., Finn, M. G. & Sharpless, K. B. Click chemistry: diverse chemical function from a few good reactions. *Angew. Chem. Int. Ed.* **40**, 2004–2021 (2001).
39. Sletten, E. M. & Bertozzi, C. R. Bioorthogonal chemistry: fishing for selectivity in a sea of functionality. *Angew. Chem. Int. Ed.* **48**, 6974–6998 (2009).
40. Agard, N. J., Prescher, J. A. & Bertozzi, C. R. A strain-promoted [3 + 2] azide-alkyne cycloaddition for covalent modification of biomolecules in living systems. *J. Am. Chem. Soc.* **126**, 15046–15047 (2004).
41. Thirumurugan, P., Matosiuk, D. & Jozwiak, K. Click chemistry for drug development and diverse chemical–biology applications. *Chem. Rev.* **113**, 4905–4979 (2013).
42. Ogba, O. M., Warner, N. C., O'Leary, D. J. & Grubbs, R. H. Recent advances in ruthenium-based olefin metathesis. *Chem. Soc. Rev.* **47**, 4510–4544 (2018).
43. Fu, L., Zhang, T., Fu, G. & Gutekunst, W. R. Relay conjugation of living metathesis polymers. *J. Am. Chem. Soc.* **140**, 12181–12188 (2018).
44. Knall, A. C. & Slugovc, C. Inverse electron demand Diels–Alder (iEDDA)-initiated conjugation: a (high) potential click chemistry scheme. *Chem. Soc. Rev.* **42**, 5131–5142 (2013).
45. Oliveira, B. L., Guo, Z. & Bernardes, G. J. L. Inverse electron demand Diels–Alder reactions in chemical biology. *Chem. Soc. Rev.* **46**, 4895–4950 (2017).
46. Blackman, M. L., Royzen, M. & Fox, J. M. Tetrazine ligation: fast bioconjugation based on inverse-electron-demand Diels–Alder reactivity. *J. Am. Chem. Soc.* **130**, 13518–13519 (2008).
47. Oh, D. Y. & Bang, Y. J. HER2-targeted therapies—a role beyond breast cancer. *Nat. Rev. Clin. Oncol.* **17**, 33–48 (2020).
48. Nakada, T., Sugihara, K., Jikoh, T., Abe, Y. & Agatsuma, T. The latest research and development into the antibody–drug conjugate, [fam-] trastuzumab deruxtecan (DS-8201a), for HER2 cancer therapy. *Chem. Pharm. Bull. (Tokyo)* **67**, 173–185 (2019).
49. Hou, Y. & Lu, H. Protein PEPylation: a new paradigm of protein–polymer conjugation. *Bioconjug. Chem.* **30**, 1604–1616 (2019).
50. Chen, P., Yun, W., Sun, T., Lin, J. & Zhang, K. Enabling safer, more potent oligonucleotide therapeutics with bottlebrush polymer conjugates. *J. Control. Release* **366**, 44–51 (2024).
51. Yu, X. et al. Reducing affinity as a strategy to boost immunomodulatory antibody agonism. *Nature* **614**, 539–547 (2023).
52. Oostindie, S. C., Lazar, G. A., Schuurman, J. & Parren, P. W. H. I. Avidity in antibody effector functions and biotherapeutic drug design. *Nat. Rev. Drug Discov.* **21**, 715–735 (2022).
53. Gall, V. A. et al. Trastuzumab increases HER2 uptake and cross-presentation by dendritic cells. *Cancer Res.* **77**, 5374–5383 (2017).
54. Geri, J. B. et al. Microenvironment mapping via Dexter energy transfer on immune cells. *Science* **367**, 1091–1097 (2020).

55. Vohidov, F. et al. Design of BET inhibitor bottlebrush prodrugs with superior efficacy and devoid of systemic toxicities. *J. Am. Chem. Soc.* **143**, 4714–4724 (2021).
56. Zafar, H., Liu, B., Nguyen, H. V. T. & Johnson, J. A. Caspase-3-responsive, fluorogenic bivalent bottlebrush polymers. *ACS Macro Lett.* **13**, 571–576 (2024).
57. Tsao, L. et al. Effective extracellular payload release and immunomodulatory interactions govern the therapeutic effect of trastuzumab deruxtecan (T-DXd). *Nat. Commun.* **16**, 3167 (2025).
58. Pyzik, M., Kozicky, L. K., Gandhi, A. K. & Blumberg, R. S. The therapeutic age of the neonatal Fc receptor. *Nat. Rev. Immunol.* **23**, 415–432 (2023).
59. Akaiwa, M., Dugal-Tessier, J. & Mendelsohn, B. A. Antibody–drug conjugate payloads; study of auristatin derivatives. *Chem. Pharm. Bull. (Tokyo)* **68**, 201–211 (2020).
60. Junutula, J. R. et al. Site-specific conjugation of a cytotoxic drug to an antibody improves the therapeutic index. *Nat. Biotechnol.* **26**, 925–932 (2008).
61. Ejigah, V. et al. Approaches to improve macromolecule and nanoparticle accumulation in the tumor microenvironment by the enhanced permeability and retention effect. *Polymers* **14**, 2601 (2022).
62. Tolcher, A. W. et al. Randomized phase II study of BR96-doxorubicin conjugate in patients with metastatic breast cancer. *J. Clin. Oncol.* **17**, 478 (1999).
63. Hendrikx, J. J. M. A. et al. Fixed dosing of monoclonal antibodies in oncology. *Oncologist* **22**, 1212 (2017).
64. Li, Y. et al. Targeted immunotherapy for HER2-low breast cancer with 17p loss. *Sci. Transl. Med.* **13**, eabc6894 (2021).
65. Burslem, G. M. & Crews, C. M. Proteolysis-targeting chimeras as therapeutics and tools for biological discovery. *Cell* **181**, 102–114 (2020).
66. Dale, B. et al. Advancing targeted protein degradation for cancer therapy. *Nat. Rev. Cancer* **21**, 638–654 (2021).
67. Wu, T. et al. Targeted protein degradation as a powerful research tool in basic biology and drug target discovery. *Nat. Struct. Mol. Biol.* **27**, 605–614 (2020).
68. Li, X. & Song, Y. Proteolysis-targeting chimera (PROTAC) for targeted protein degradation and cancer therapy. *J. Hematol. Oncol.* **13**, 50 (2020).
69. Raina, K. et al. PROTAC-induced BET protein degradation as a therapy for castration-resistant prostate cancer. *Proc. Natl Acad. Sci. USA* **113**, 7124–7129 (2016).
70. Noblejas-López, M. et al. Activity of BET-proteolysis targeting chimeric (PROTAC) compounds in triple negative breast cancer. *J. Exp. Clin. Cancer Res.* **38**, 383 (2019).
71. Sun, X. et al. A chemical approach for global protein knockdown from mice to non-human primates. *Cell Discov.* **5**, 10 (2019).
72. Noblejas-López, M. et al. MZ1 co-operates with trastuzumab in HER2 positive breast cancer. *J. Exp. Clin. Cancer Res.* **40**, 106 (2021).
73. Dragovich, P. S. Degrader-antibody conjugates. *Chem. Soc. Rev.* **51**, 3886–3897 (2022).
74. Chen, W. et al. MUC1: structure, function, and clinic application in epithelial cancers. *Int. J. Mol. Sci.* **22**, 6567 (2021).
75. Cheever, M. A. et al. The prioritization of cancer antigens: a National Cancer Institute pilot project for the acceleration of translational research. *Clin. Cancer Res.* **15**, 5323–5337 (2009).
76. Liu, B. et al. An organometallic swap strategy for bottlebrush polymer–protein conjugate synthesis. *Chem. Commun.* **60**, 4238–4241 (2024).
77. Hamblett, K. J. et al. Effects of drug loading on the antitumor activity of a monoclonal antibody drug conjugate. *Clin. Cancer Res.* **10**, 7063–7070 (2004).
78. Bai, S. et al. Cylindrical polymer brushes-anisotropic unimolecular micelle drug delivery system for enhancing the effectiveness of chemotherapy. *Bioact. Mater.* **6**, 2894–2904 (2021).
79. Rabanel, J. M. et al. Deep tissue penetration of bottle-brush polymers via cell capture evasion and fast diffusion. *ACS Nano* **16**, 21583–21599 (2022).
80. Strasser, P. et al. Degradable bottlebrush polypeptides and the impact of their architecture on cell uptake, pharmacokinetics, and biodistribution in vivo. *Small* **19**, 2300767 (2023).
81. Qi, Y. et al. A brush-polymer/exendin-4 conjugate reduces blood glucose levels for up to five days and eliminates poly(ethylene glycol) antigenicity. *Nat. Biomed. Eng.* **1**, 0002 (2016).
82. Gil Alvaradejo, G. et al. Polyoxazoline-based bottlebrush and brush-arm star polymers via ROMP: syntheses and applications as organic radical contrast agents. *ACS Macro Lett.* **8**, 473–478 (2019).
83. Shieh, P., Nguyen, H. V. T. & Johnson, J. A. Tailored silyl ether monomers enable backbone-degradable polynorbornene-based linear, bottlebrush, and star copolymers through ROMP. *Nat. Chem.* **11**, 1124–1132 (2019).

Methods

ABC conjugation and purification

ABCs were prepared by incubation of BP-Tz and Ab-TCO at different ratios in PBS at room temperature for 24 hours. The synthesis details of the BT-Tz and Ab-TCO are described in Supplementary Information Section 2. The conjugation was monitored by SDS-PAGE. ABCs were purified by fast protein liquid chromatography (FPLC) with a cationic exchange column or size exclusion column. The details for ABC purification through FPLC are described below. The crude reaction mixtures were filtered through sterile 0.2-µm filters. FPLC analyses were performed on a Bio-Rad NGC Quest 10 Plus system with Bio-Rad ENrich SEC 70 or SEC 650 columns at a flow rate of 1 ml min^{-1} with 1× PBS buffer as the mobile phase and a Cytiva HiTrap SP HP cationic exchange column (5 ml) attached separately at a flow rate of 5 ml min^{-1} with 0.02 M acetate buffer (pH 4.5) as the mobile phase. Finally, the conjugates were concentrated, and the salt was removed by ultracentrifugation with molecular weight cutoff = 10,000.

Descriptions of assays used for ABC characterization

Payload release assay. Stock solutions of macromonomers were prepared in PBS at 5 mg ml^{-1}. Aliquots of 100 µl of these solutions were then added to 2 ml liquid chromatography–mass spectrometry (LC–MS) vials. The vials were incubated at 37 °C in an oven. At predetermined timepoints, one vial was removed from the oven and allowed to cool to room temperature. Then, 100 µl of DMSO was added, and the resulting sample was analyzed by LC–MS.

SDS-PAGE gel. Samples were mixed with 4× non-reducing loading buffer. Specifically, 9 µl of each sample (mAb, crude or purified ABCs) was mixed with 3 µl of loading buffer, and each sample was loaded on an acrylamide gel for gel electrophoresis.

ELISA assays. ELISA assays were performed using 96-well plates coated with tag-free Human HER2 (ACROBiosystems) at 1 µg ml^{-1} (100 µl per well) in coating buffer (pH 9.4 bicarbonate buffer; Thermo Fisher Scientific). Samples were incubated for 1 hour, with the highest concentration being 40 µg ml^{-1}. Blocking solution was 2% BSA in 0.05% Tween 20 in TBS (pH 7.4) (Thermo Fisher Scientific); washing solution was 0.05% Tween 20 in TBS (pH 7.4); antibody and sample buffer were 0.5% BSA in 0.05% Tween 20 in TBS (pH 7.4); detection antibody was Peroxidase AffiniPure Goat Anti-Human IgG (Jackson ImmunoResearch); substrate solution (Thermo Fisher Scientific) was used following the manufacturer's protocol (mix equal volumes of the TMB solution and the peroxide solution); and 2 M H_2SO_4 was used as stop solution. Data were acquired using a Tecan M200.

MST binding assays. MST assays were performed on a Monolith instrument (NanoTemper) following the manufacturer's protocol (https://www.qd-taiwan.com/products/nanotemper.html). The highest concentration of sample used was 250 nM. The fluorescent HER2 was generated using His-Tag Human HER2 (ACROBiosystems) and the corresponding His-Tag labeling kit RED-tris-NTA (NanoTemper). The labeling reaction was done in PBS, and the incubation time was 30 minutes.

FcRn binding assays. FcRn assays were performed using the Lumit FcRn Binding Immunoassay (Promega) following the manufacturer's protocols. Sample pH was adjusted to 6.0, and the control antibody standards covered an IgG concentration range of 0.004–4,000 µg ml^{-1} (pre-dilution). Then, 25 µl of Tracer-LgBiT solution, 25 µl of control antibody or sample and 50 µl of hFcRn-SmBiT solution were added into the wells of a white 96-well plate sequentially. The plate was covered with a plate seal and mixed gently on a plate shaker (300–400 r.p.m.) for 45 minutes at room temperature. Next, 3 ml of FcRn assay buffer and 60 µl of Lumit FcRn detection substrate A were mixed into a reservoir to create Lumit FcRn detection reagent. Then, 25 µl of Lumit FcRn detection reagent from the reservoir was added to each plate well. The plate was incubated at room temperature for 5 minutes, after which the plate was read on a Tecan M200 luminometer to acquire the data.

Cell studies

Cell culture. BT-474 (clone 5), SKBR-3, SKOV-3, MCF-10A, HCC-70 and CAOV-3 cells were cultured and used in the present work. BT-474 cells were grown in RPMI 1640 supplemented with 5% FBS, 100 U ml^{-1} penicillin, 100 µg ml^{-1} streptomycin and 2 mM L-glutamine and incubated in a humidified 37 °C, 5% CO_2 incubator. SKOV-3, MCF-10A, CAOV-3 and HCC-70 cells were grown in DMEM:F12 media supplemented with 5% FBS, 100 U ml^{-1} penicillin, 100 µg ml^{-1} streptomycin and 2 mM L-glutamine and incubated in a humidified 5% CO_2 incubator at 37 °C. SKBR-3 cells were grown in McCoy's media supplemented with 10% FBS, 100 U ml^{-1} penicillin and 100 µg ml^{-1} streptomycin and grown at 37 °C in a 5% CO_2 incubator.

Flow cytometry. To evaluate selective cell targeting abilities, Cy5.5 (1% or 5%) dye-labeled materials (BPD, control ABC or ABC) were used for fluorescence. Different cells (BT-474, SKBR-3, SKOV-3, MCF-10A and CAOV-3) were treated with BPD, control ABC or ABC at different concentrations in 0.2 million cells in 0.2 ml of media at 37 °C in a 5% CO_2 incubator. The cells were then washed twice with PBS, stained with Zombie Yellow, washed and resuspended in fluorescence-activated cell sorting (FACS) buffer. The samples were then subjected to flow cytometry on a BD FACSymphony A3, and the data collected were analyzed on a FACSDiva (version 9.0) and with FlowJo (version 10.9) software. A representative FACS gating strategy for flow cytometry analysis is shown in Supplementary Fig. 19.

Cytotoxicity assays. Different cells (including MCF-10A, SKOV-3, SKBR-3, BT-474 and CAOV-3) were seeded into 96-well tissue culture plates at a density of 15,000 cells per well per 100-µl sample and incubated at 37 °C. After 24 hours, the culture media were replaced, and the cells were treated with different concentrations of ABCs, controls or BPD samples in 100 µl of media (10-µl sample solution with different concentrations + 90 µl of medium). At the desired time interval (24 hours, 48 hours, 72 hours or 5 days), the medium was removed, and the cells were cultured in 100 µl of 10% MTT (5 mg ml^{-1}) in a medium solution for another 4 hours. Then, the solution was discarded, and the remaining crystals were dissolved in 100 µl of DMSO. The solution was subjected to absorbance measurement with SpectraMax M3 at 590 nm. Cell death was measured by the MTT assay in triplicate. To enhance targeting efficiency, cytotoxicity assays can be performed by incubating cells with samples for a specific period (for example, several hours to 1–2 days), followed by replacing the drug-containing media with fresh media and continuing incubation for an additional 2–4 days.

Confocal microscopy. Cell internalization studies were performed with BT-474 cells, seeded at 150,000 cells per milliliter in glass-bottomed Petri dishes and cultured for 24 hours at 37 °C in a 5% CO_2 incubator. Cells were washed three times with PBS buffer and incubated with 1 ml of media containing ABC, BPD or control ABC with different concentrations at 37 °C for different times (for example, 10 minutes, 30 minutes or 4 hours). Then, the media were replaced with fresh stock, and the cells were further incubated at different times (for example, 0 hours, 24 hours and 72 hours). Afterwards, the cells were washed three times with PBS buffer. Then, the cell nucleus was stained with or without Hoechst 33342 (8 µM), and the cell membrane was stained with CellMask Green for confocal laser scanning microscopy (CLSM) analysis. In addition, for the drug release experiment, SN-38-HER2 ABC was incubated with the precultured cells in glass-bottomed Petri dishes for 4 hours. Then, the media were replaced with fresh stock, and the cells were incubated at different times (for example, 0 hours, 24 hours and 72 hours) for CLSM analysis. Live-cell imaging was performed using a Nikon Spectral A1R confocal microscope.

Proteomics studies. *Labeling reagents and iridium photocatalyst-conjugated ABC generation*. Biotin–PEG3–diazirine probe and Ir-G3 DBCO photocatalyst were prepared as previously described[84,85]. The Ir-G3 DBCO catalyst was conjugated to either trastuzumab or IgG1 pre-functionalized with NHS–PEG3–azide (BroadPharm, BP-21605) using previously described methods[85]. Then, the surfaces of the Ir-conjugated antibodies were modified with TCO functionality through the reaction with TCO–PEG12–NHS according to Supplementary Information Section 2.4. PEG-based BP-Tz (degrees of polymerization = 60) was conjugated onto these antibodies for PEG-HER2^{Ir} or PEG-IgG1^{Ir} ABCs. These ABCs were purified by FPLC according to Supplementary Information Section 2.5.

µMap proximity labeling with ABCs. BT-474 cells were seeded onto 10-cm dishes with three biological replicates for each condition and grown to approximately 90% confluency on the day of labeling. Cell media were gently aspirated, and dishes were then rinsed (0.5 m) and then incubated (1 ml) with 0.05% trypsin-EDTA (Thermo Fisher Scientific, 23500054) until cells detached from dishes. Cells were resuspended in complete media and transferred to 15-ml conical centrifuge tubes (Olympus Plastics, 28-101). Samples were centrifuged at 400*g* for 3 minutes at 4 °C in a Sorvall Legend XTR (Thermo Fisher Scientific, 75004521). The supernatant was gently aspirated, and cells were resuspended in 1 ml of ice-cold DPBS (Thermo Fisher Scientific, 14190144) and transferred to 1.5-ml Axygen Maxymum Recovery tubes (MCT-150-LC). Cell suspensions were centrifuged using the same conditions and resuspended in 1 ml of fresh, ice-cold DPBS. Samples were then incubated with 5 µg of either PEG-HER2^{Ir} or PEG-IgG1^{Ir} and incubated in the dark with rotation at 4 °C for 1 hour. Samples were then centrifuged and washed three times in 1 ml of ice-cold DPBS before being resuspended in 1 ml of ice-cold 250 µM Biotin–PEG3–diazirine in DPBS. Samples were incubated in the dark with rotation at 4 °C for 10 minutes and then irradiated at 4 °C with M2 photoreactors (Acceled; outfitted with a 450-nm LED plate, 100% intensity, corresponding to an output of 2.2 W). Samples were then washed two times in 1 ml of ice-cold DPBS. Samples were then lysed and prepared for proteomics as previously detailed[86].

MS-based proteomics and data analysis. Label-free, data-independent acquisition (DIA) proteomics was performed using a Bruker timsTOF Pro 2 connected to a nanoElute LC. For each sample, approximately 100 ng of protein was injected onto a trap column (C18 PepMap; 5-µm particle size, 5-mm length and 300-µm internal diameter), followed by separation via an analytical column (C18 ReproSil AQ; 1.9-µm particle size, 100-mm length and 75-µm internal diameter). Peptides were eluted via an acetonitrile/water gradient at a column temperature of 40 °C (buffer A = 0.1% formic acid/water, buffer B = 0.1% formic acid/acetonitrile; flow rate = 0.5 µl min^{-1}; gradient start at 2% buffer B and then increase to 35% buffer B over 20 minutes and then increase to 95% buffer B over 0.5 minutes and hold at 95% buffer B for 2.25 minutes). Scans were performed in positive ion, dia-PASEF (parallel accumulation serial fragmentation) mode over an *m/z* range of 100–1,700 with a ramp time of 100 ms, accumulation time of 100 ms and a duty cycle of 100% ramp rate of 9.43 Hz, MS averaging set to 1. Absolute thresholds were set to 5,000 for mobility peaks and 10 for MS peaks. Data were collected with Bruker Compass HyStar version 6.2.

The resulting raw data (.d files) were then processed via DIA-NN 1.8.1 (refs. 87,88) with the following parameters: trypsin/P digestion three missed cleavages, three maximum variable modifications—N-term M excision, Ox(M), Ac(N-term) and C-carbamidomethylation—peptide length range 7–30, precursor charge range 1–4, *m/z* range 300–1,800, fragment ion range 200–1,800, mass accuracy and MS accuracy both set to 10 and precursor false discovery rate set to 1%. Within the DIA-NN algorithm, the following settings were applied: 'use iso-topologues', 'MBR' (match between runs), 'no shared spectra' and 'heuristic protein inference'. A spectral library was used, which was generated in DIA-NN from all known human proteins (in silico spectral library—generated in DIA-NN via FASTA of UniProt human proteome UP000005640; options selected were 'FASTA digest for library-free search/library generation' and 'deep learning-based spectra, retention times and ion mobilities prediction'; other parameters were the same as described above). After processing, the resulting matrix .pg files were worked up in Perseus (version 2.0.7.0)[89], where intensities were inputted as 'main' while the other descriptors were listed as 'categorical'. Intensities were transformed by $\log_2$, and data were annotated to the appropriate condition (either PEG-HER2^{Ir} or PEG-IgG1^{Ir}). Here, missing values were then replaced from a normal distribution (width = 0.3, downshift = 1.8, separately for each column). Normalization was performed via median subtraction, and a volcano plot was generated using a *t*-test for statistical significance. Contaminants were filtered manually for image clarity. The resulting volcano plot was plotted in GraphPad Prism 9.5 for the final figure. HER2 interactome comparison was performed through cross-referencing with BioGRID version 4.4.237.

Animal studies

Animal usage. All experiments involving animals were reviewed and approved by the Massachusetts Institute of Technology (MIT) Committee for Animal Care. All mice were housed in a specific pathogen-free facility under standard conditions, including a 12-hour light/dark cycle, ambient temperature maintained at approximately 18–26 °C and relative humidity of 30–70%. In vivo tumor imaging of the subcutaneous model (BT-474 and CAOV-3 cell lines; NCR nude mouse (female), Taconic) was performed at the Imaging Facility Center of the Koch Institute for Integrative Cancer Research at MIT. NCR nude mice (female, 8–12 weeks old, Taconic; $n = 3$–4 mice per group) were used for pharmacokinetic and biodistribution studies. All animals received an alfalfa-free diet (TestDiet) at least 2 weeks before the start of the studies to minimize autofluorescence. No estrogen was used for these experiments.

Subcutaneous and orthotopic tumor models. NCR nude mice (female, 8–12 weeks old, Taconic) were used for the generation of the xenograft cancer models. Mice were injected subcutaneously (BT-474 and CAOV-3 cells) or orthotopically (HCC-70 cells) with 2 million cells. Tumor growth was monitored for 2–4 weeks until appropriate cumulative diameters (approximately 1 cm) were achieved. Tumor-bearing mice were then randomly distributed to receive different treatments ($n = 5$–8 mice per group).

Pharmacokinetics and biodistribution studies. ABC and BPD solutions (5.0 mg in PBS, injected as 0.25 ml of a 20 mg ml^{-1} solution) were prepared, passed through sterile 0.2-µm filters (Nalgene, PES membrane) and administered into NCR nude mice ($n = 3$ per group) via intravenous or intraperitoneal injection. Blood samples were taken at a predetermined timepoint of up to 72 hours after administration via cardiac puncture after euthanasia in a CO_2 chamber. The blood samples were subjected to fluorescence imaging (IVIS, Cy5.5 l_{ex}/l_{em} = 640/700 nm) for analysis of blood compartment pharmacokinetics, which was then fitted into a two-component model using standard procedures[2,7]. To determine biodistribution profiles, organs from these same NCR nude mice were harvested and subjected to fluorescence imaging (IVIS, Cy5.5 l_{ex}/l_{em} = 640/700 nm).

In vivo efficacy studies. BT-474, HCC-70 and CAOV-3 cells were cultured following the protocol described above to a final confluency of 80%. Cells were then harvested, mixed with Geltrex (for BT-474 and CAOV-3 cells) or Matrigel (for HCC-70 cells) and sterile pH 7.4 PBS buffer (1:1), filtered through sterile 0.2-µm filters and injected subcutaneously (2.0×10^6 cells) into the hind flank of NCR nude mice (for BT-474 and CAOV-3 cells) or orthotopically into the fourth mammary pad

(for HCC-70 cells). Tumor growth was monitored for 1–3 weeks until appropriate cumulative diameters (approximately 1 cm, measured by a digital caliper) were achieved. Tumor-bearing mice were then randomized into groups of $n = 5–8$ and given intravenous or intraperitoneal injections of 100 µl of materials at varying concentrations (to give 5 mg kg^{-1} mAb) with different administration schedules as illustrated in the figures of the main text. Tumor growth was then assessed via caliper measurements. We note that, given the relatively low potency and established safety of BPDs on their own, and, for convenience, we used ABCs prepared directly from mAb conjugation reactions, without subsequent separation of unconjugated BPD (approximately 30%), for in vivo efficacy studies. The doses stated in the text include this excess BPD; thus, with further purification to remove BPDs, it is expected that these constructs may perform similarly at lower total payload doses. The exception to this practice was in the studies comparing ABCs to T-DXd, where the ABCs were rigorously separated from BPD.

Statistics and reproducibility. In vitro and in vivo signals measured from ABCs, control ABCs and BPDs are reported as mean ± s.e.m. Statistical analysis was done using a two-tailed *t*-test. Results from representative experiments, such as micrographs, were independently repeated with similar outcomes. Specifically, Fig. 1e was reproduced in three independent experiments; Fig. 1f was reproduced in two independent experiments; Fig. 1h was reproduced in three independent experiments; and Fig. 1j was reproduced in two independent experiments.

Reporting summary

Further information on research design is available in the Nature Portfolio Reporting Summary linked to this article.

Data availability

All data supporting the findings of this study are available within the article, in its supplementary information and on figshare (https://doi.org/10.6084/m9.figshare.29414048)[90] and can be obtained from the corresponding authors upon reasonable request. Source data are provided with this paper.

References

84. Trowbridge, A. D. et al. Small molecule photocatalysis enables drug target identification via energy transfer. *Proc. Natl Acad. Sci. USA* **119**, e2208077119 (2022).
85. Oakley, J. V. et al. Radius measurement via super-resolution microscopy enables the development of a variable radii proximity labeling platform. *Proc. Natl Acad. Sci. USA* **119**, e2203027119 (2022).
86. Pan, C., Knutson, S. D., Huth, S. W. & MacMillan, D. W. C. µMap proximity labeling in living cells reveals stress granule disassembly mechanism. *Nat. Chem. Biol.* **21**, 490–500 (2025).
87. Demichev, V., Messner, C. B., Vernardis, S. I., Lilley, K. S. & Ralser, M. DIA-NN: neural networks and interference correction enable deep proteome coverage in high throughput. *Nat. Methods* **17**, 41–44 (2020).
88. Demichev, V. et al. dia-PASEF data analysis using FragPipe and DIA-NN for deep proteomics of low sample amounts. *Nat. Commun.* **13**, 3944 (2022).
89. Tyanova, S. et al. The Perseus computational platform for comprehensive analysis of (prote)omics data. *Nat. Methods* **13**, 731–740 (2016).
90. Liu, B. et al. Data for 'antibody-bottlebrush prodrug conjugates for targeted cancer therapy'. figshare. https://doi.org/10.6084/m9.figshare.29414048 (2025).

Acknowledgements

We thank the National Institutes of Health (2R01CA220468-06A1) and the Yosemite–American Cancer Society Award (YACS-24-1343208-01-YACS) for support. B.L. thanks the Ludwig Center of the Koch Institute for Integrative Cancer Research at MIT for a postdoctoral fellowship and the Koch Institute Frontier Research Program for support. P.M. would like to acknowledge support from the National Science Foundation Graduate Research Fellowship Program (NSF-GRFP, grant no. 2141064). Z.H.B., P.A.R. and D.W.C.M. are thankful for the financial support provided by the National Institutes of Health, National Institute of General Medical Sciences (R35GM134897-04); the Princeton Catalysis Initiative; Princeton University; and kind gifts from Merck, Janssen, Bristol Myers Squibb, Genentech, Genmab and Pfizer. N.J. is supported by the US Department of Defense (DOD award W81XWH-22-1-1122). We are grateful for the use of open-access tools, including DIA-NN, Perseus and BioGRID.

Author contributions

B.L. and J.A.J. conceived the project idea. B.L. designed and performed the polymerization and bioconjugation. B.L. and H.V.-T.N. synthesized and characterized the macromonomers. B.L. performed the in vitro experiments. B.L., H.V.-T.N. and Y.J. performed the in vivo experiments. A.X.W., V.L., Z.S., Y.D., P.L.M., Y.W., W.W., S.B., S.H., P.S., S.L.K. and M.B. assisted with the experiments. Z.H.B. and P.A.R. performed µMap optimization and proteomic analysis, under the guidance of D.W.C.M. N.J., M.D. and R.M.E. provided the site-specific thiol-mAb. J.A.J. supervised the research. B.L. and J.A.J. analyzed the data and wrote the manuscript, and all authors discussed and commented on it.

Competing interests

J.A.J., H.V.-T.N. and Y.J. are shareholders of Window Therapeutics. D.W.C.M. declares an ownership interest in Dexterity Pharma, which has commercialized materials used in this work. The remaining authors declare no competing interests.

Additional information

Extended data is available for this paper at https://doi.org/10.1038/s41587-025-02772-z.

Supplementary information The online version contains supplementary material available at https://doi.org/10.1038/s41587-025-02772-z.

Correspondence and requests for materials should be addressed to Jeremiah A. Johnson.

Peer review information *Nature Biotechnology* thanks Charles Dumontet and the other, anonymous, reviewer(s) for their contribution to the peer review of this work.

https://doi.org/10.1038/s41587-025-02772-z

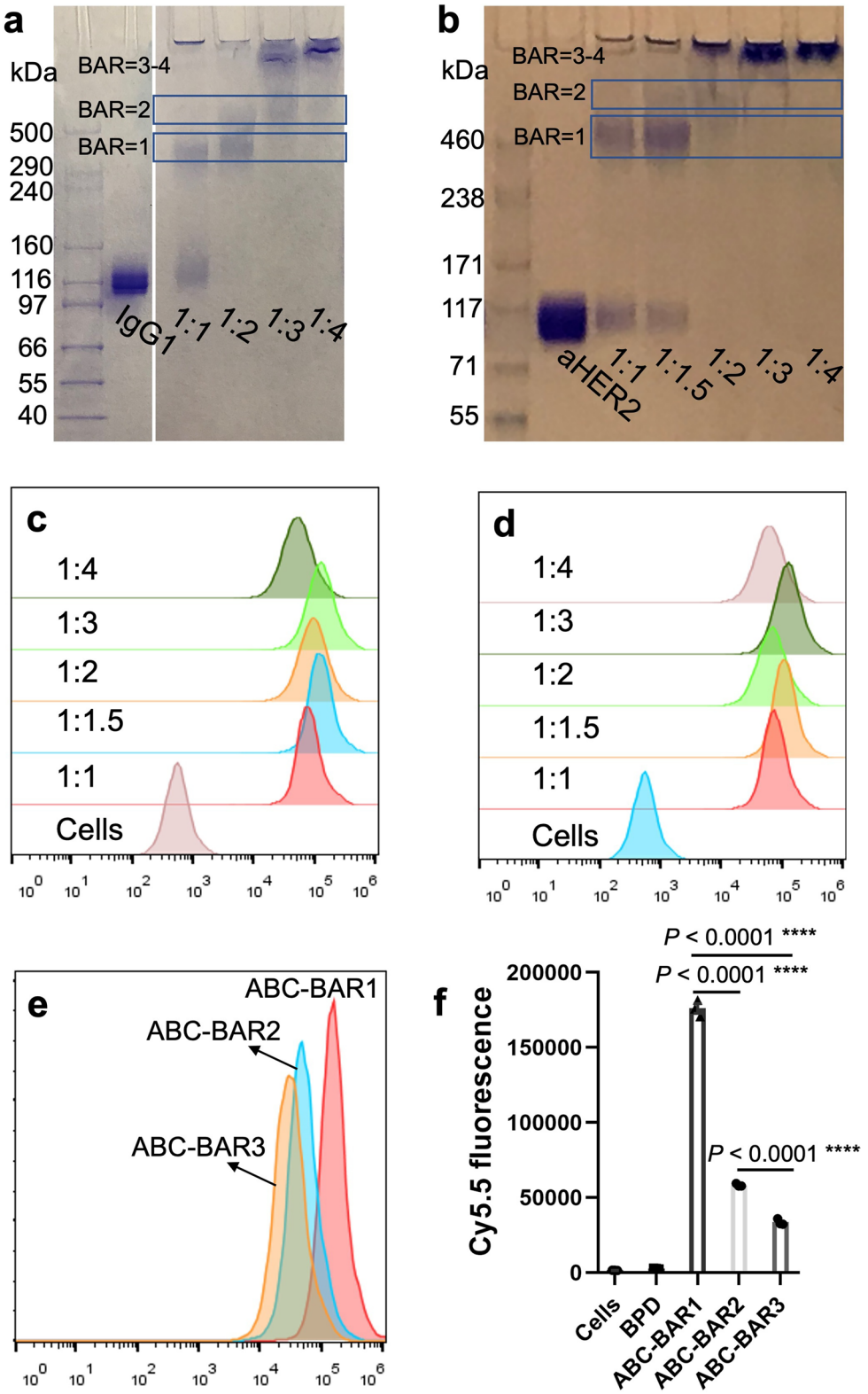

Extended Data Fig. 1 | ABC synthesis using different stoichiometries of BP-Tz and Ab-TCO. a. Non-reducing SDS-PAGE analysis of model IgG1-based ABCs as a function of synthesis stoichiometry. BAR = average brush–antibody ratio. **b**. Non-reducing SDS-PAGE analysis of Trastuzumab-based ABCs as a function of synthesis stoichiometry. **c**. Flow cytometry histograms showing Cy5.5-HER2 uptake into HER2 + BT-474 cells as a function of synthesis stoichiometry (that is, the constructs are present as a mixture of BAR values). The *x*-axis represents the Cy5.5 fluorescence intensity. Since the number of Cy5.5 dyes per ABC increases with BAR, histograms are normalized to the total Cy5.5 loading for each construct to enable comparison (normalized to 40 μg/mL Cy5.5-BP, 1 h). **d**. Flow cytometry histograms for the same constructs shown in panel **c** normalized by antibody dose (normalized to 10 μg/mL mAb, 1 h). The *x*-axis represents the Cy5.5 fluorescence intensity. **e**. and **f**. Flow cytometry histograms for BT-474 cell uptake of *isolated* Cy5.5-HER2 ABCs with different BAR values (25 μg/mL, 1 h) (that is, ABCs with each BAR were separated from the synthesis mixture). Results are presented as mean ± SEM ($n = 3$ biological replicates). Statistical analysis was done using a 2-tailed *t*-test. For these statistical tests, **** denotes $P < 0.001$.

https://doi.org/10.1038/s41587-025-02772-z

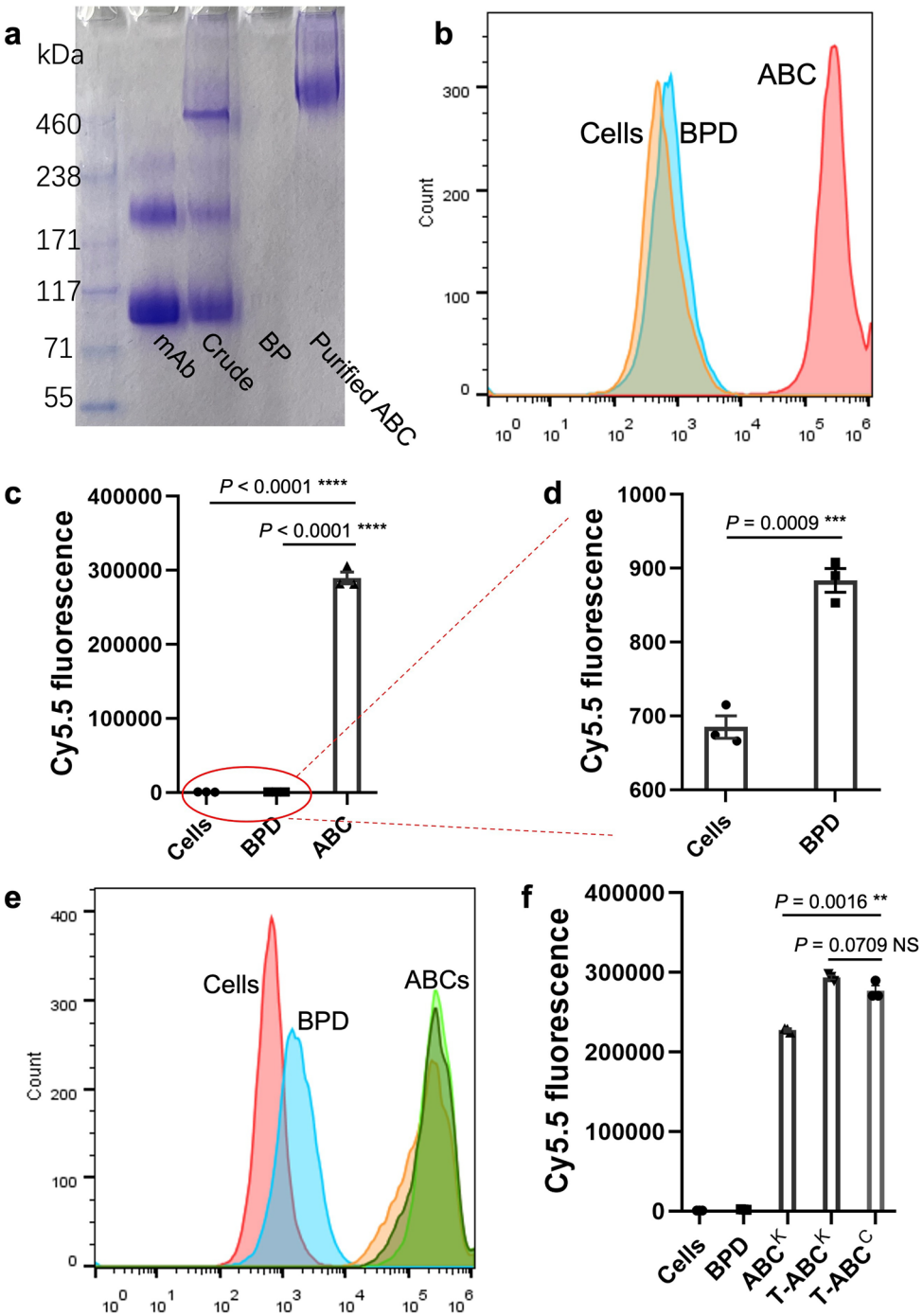

Extended Data Fig. 2 | HER2-targeted ABCs synthesized via site-specific cysteine conjugation. a. Non-reducing SDS-PAGE analysis of site-specifically conjugated Cy5.5-HER ABCs. Two independent experiments were performed with similar results. **b**. Flow cytometry histograms showing enhanced BT474 cell uptake for site-specific Cy5.5-HER2 ABC compared to BPD alone. The *x*-axis represents the Cy5.5 fluorescence intensity. **c**. and **d**. Quantification of cell uptake based on mean fluorescence intensity from flow cytometry ($n = 3$ biological replicates). **e**. and **f**. Flow cytometry histograms (The *x*-axis represents the Cy5.5 fluorescence intensity) and quantification, respectively, for cell uptake studies comparing site-specific Cy5.5-HER2 to stochastically functionalized lysine-based Cy5.5-HER2 ABC with BAR of 1 (BT474 cells, 20 µg/mL, 60 min incubation). Both ABCs have the same 5% Cy5.5 concentration. ABC^K is the lysine-conjugated Cy5.5-HER2 ABC prepared from commercial Trastuzumab. We note that this ABC was stored at 4 °C for ~1.5 years prior to this study, demonstrating excellent long-term storage stability. T-ABC^K is a stochastic Lys conjugate prepared using the engineered Trastuzumab designed for cysteine conjugation; this construct is designed to rule out differences in cell uptake between Lys-conjugated commercial Trastuzumab and the engineered antibody. Finally, T-ABC^C is the site-specific cysteine conjugate Cy5.5-HER2. Results are presented as mean ± SEM ($n = 3$ biological replicates). Statistical analysis was done using a 2-tailed *t*-test. For these statistical tests, NS denotes non-significant; **, $P < 0.01$.

https://doi.org/10.1038/s41587-025-02772-z

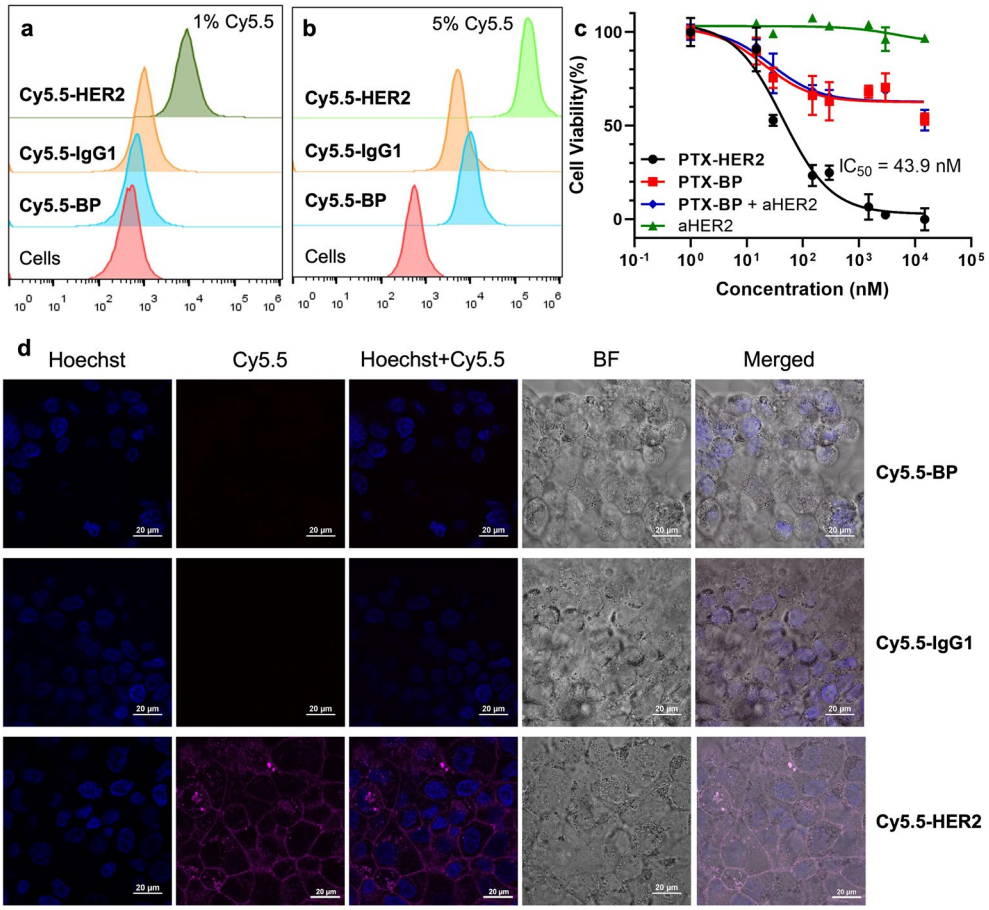

Extended Data Fig. 3 | HER2+BT474 cell uptake and toxicity experiments comparing C5.5-labeled constructs. a. Cell uptake studies comparing Cy5.5-HER2 to non-targeted controls Cy5.5-IgG1 and Cy5.5-BP, each containing 1% Cy5.5 loading (40 μg/mL, 60 min incubation, BAR = 3 for ABCs). The *x*-axis represents the Cy5.5 fluorescence intensity. **b**. Cell uptake for similar constructs with 5% Cy5.5 loadings (40 μg/mL, 60 min incubation, BAR = 3 for ABCs). The *x*-axis represents the Cy5.5 fluorescence intensity. **c**. Cytotoxicity of PTX-HER2 ABC compared to non-targeted PTX-BP (BPD only), a mixture of PTX-BPD and Trastuzumab (aHER2), and Trastuzumab (aHER2) alone for 24 h incubation. Results are presented as mean ± SEM ($n = 3$ biological replicates). The ABC PTX-HER2 displays improved cytotoxicity compared to controls. **d**. Confocal fluorescence microscopy images showed greater cell engagement and uptake for Cy5.5-HER2 compared to non-targeted controls (50 μg/mL, 6 h incubation, 1% Cy5.5 labeled ABC). Two independent experiments were performed with similar results.

https://doi.org/10.1038/s41587-025-02772-z

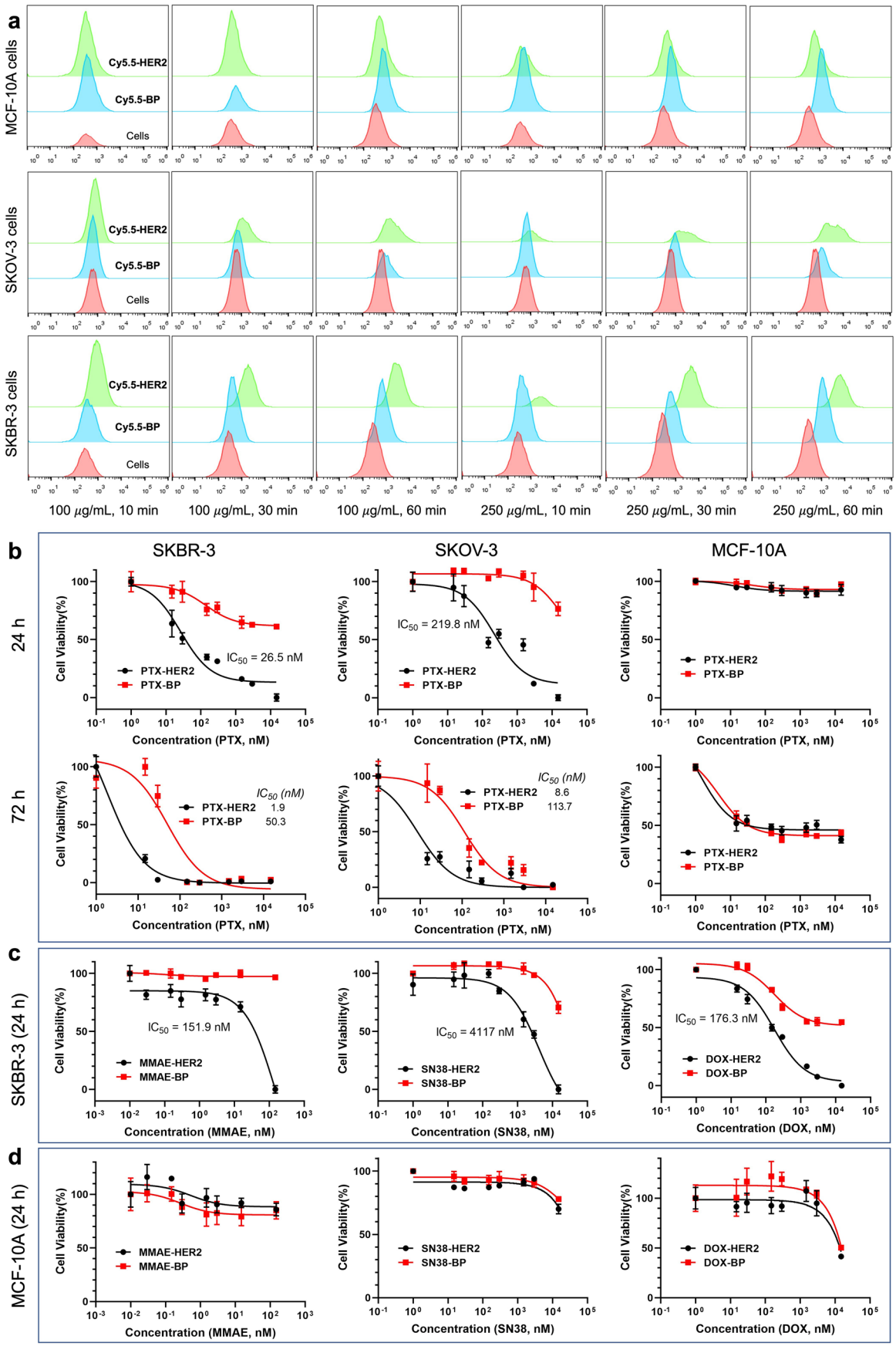

Extended Data Fig. 4 | See next page for caption.

https://doi.org/10.1038/s41587-025-02772-z

Extended Data Fig. 4 | In vitro targeting abilities of ABCs across cell lines with different HER2 expression. a) Flow cytometry histograms demonstrating that Cy5.5-HER2 ABC uptake is dependent on HER2 expression. The *x*-axes represents the Cy5.5 fluorescence intensity. Cell uptake was studied using cell lines with varied HER2 expression: MCF-10A (HER2−); SKOV-3 (HER2 medium); SKBR-3 (HER2 high). Cells were treated with Cy5.5-HER2 ABC or non-targeting Cy5.5-BP polymer (1% Cy5.5 labeling) under the conditions listed at the bottom of the figure (varied times and concentrations). **(b-d)** Cytotoxicity results for HER2-targeted ABCs comprising different payloads in cell lines with varied HER2 expression. Results are presented as mean ± SEM ($n = 3$ biological replicates). **b**. MTT assay results for PTX-HER2 compared to non-targeted PTX-BP in HER2 high, medium, and negative (from left to right), respectively, cell lines following 24 h and 72 h incubation. **c**. HER2 + SKBR3 cell viability results for ABCs with different payloads (from left to right: MMAE, SN-38, and DOX). **d**. HER2− MCF-10A cell viability results for ABCs with different payloads (from left to right: MMAE, SN-38, and DOX).

https://doi.org/10.1038/s41587-025-02772-z

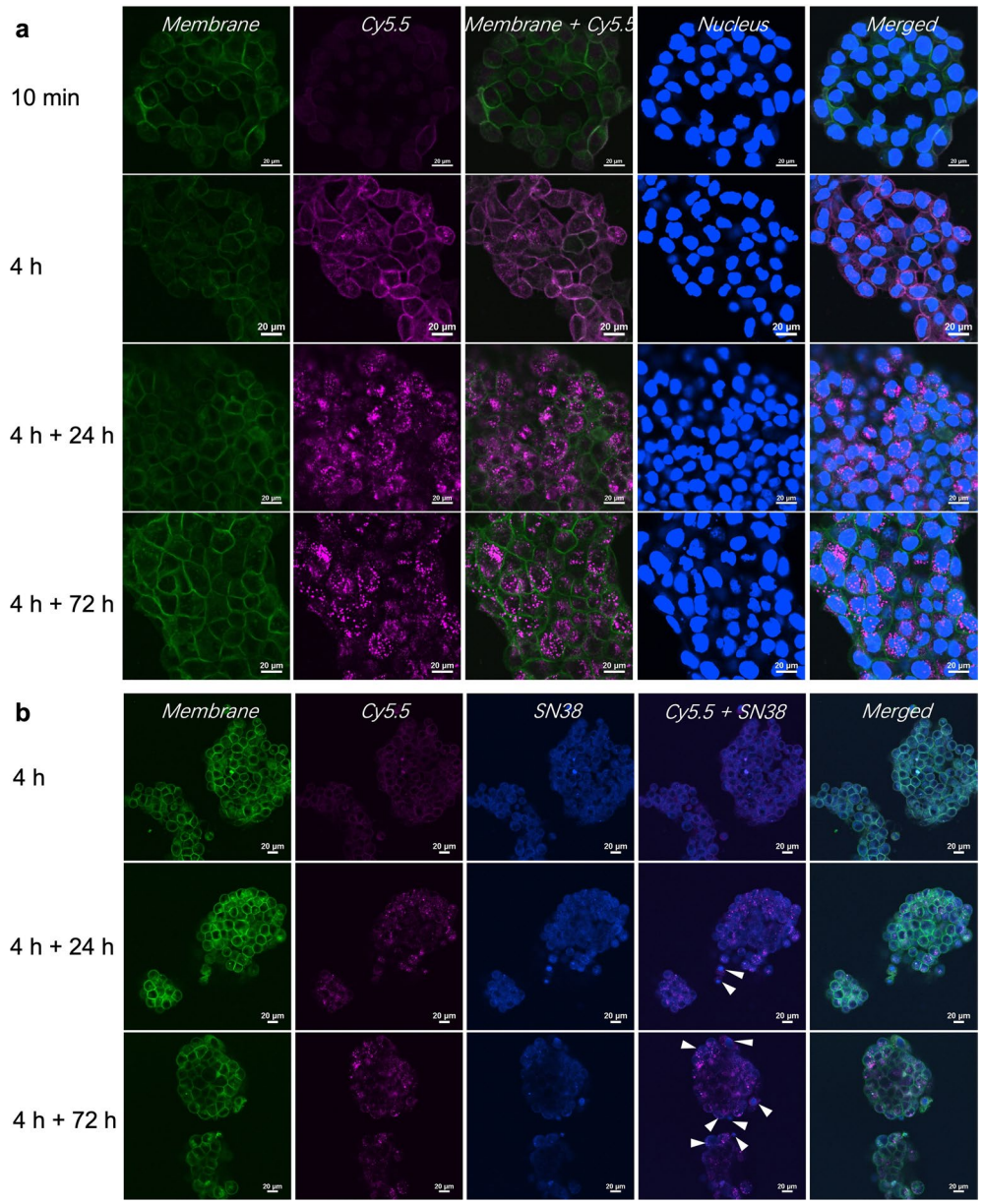

Extended Data Fig. 5 | Imaging of cell uptake and payload release in BT-474 cells. a. Confocal fluorescence images of BT-474 cells incubated with Cy5.5-HER2 (20 μg/mL) for different times. **b**. Confocal fluorescence images of BT-474 cells incubated with "theranostic" ABC SN38-Cy5.5-HER2 (50 μg/mL) for different times. White arrows point to cell nuclei where SN38 has localized following release from the ABC. In panels **a** and **b**, 4 h + 24 h and 4 h + 72 h mean that the cells were incubated with Cy5.5-HER2 or SN38-Cy5.5-HER2, respectively, for 4 h. Then, the cells were washed with PBS buffer three times and further incubated for an additional 24 h or 72 h before imaging. Two independent experiments were performed with similar results.

https://doi.org/10.1038/s41587-025-02772-z

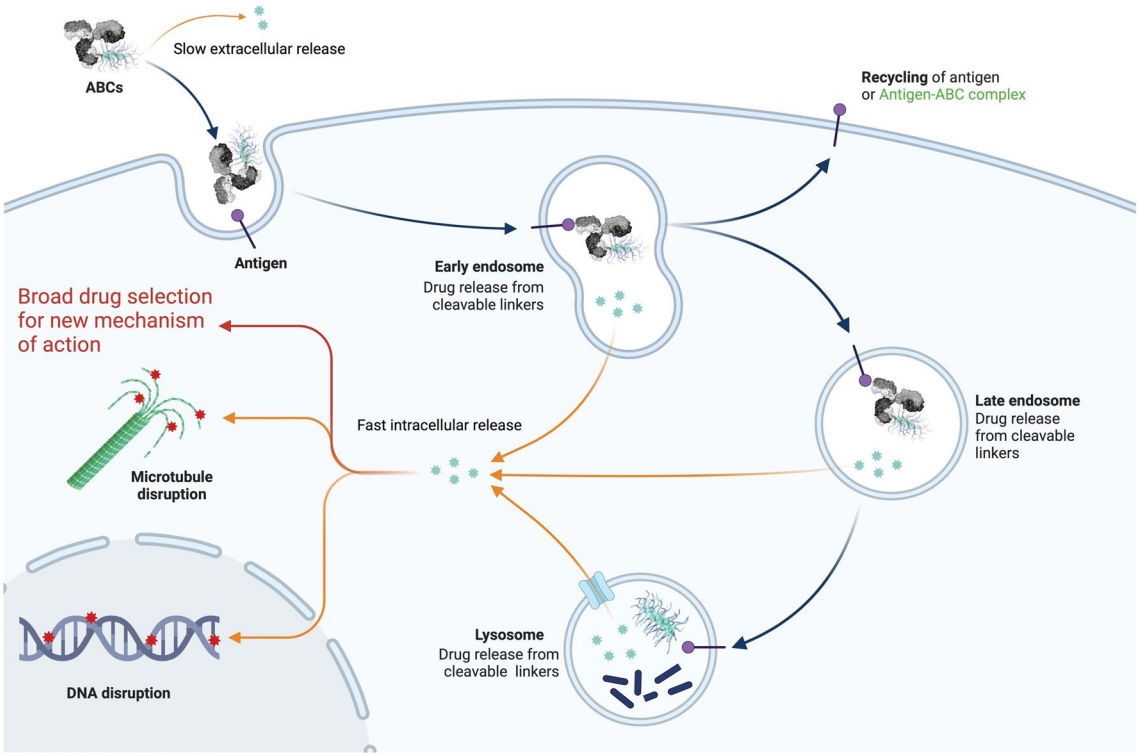

Extended Data Fig. 6 | Proposed ABC cell uptake and drug release mechanism. First, ABCs bind to the cell surface through antibody-antigen interactions (upper left). Then, bound ABCs enter the cells through receptor-mediated endocytosis. Inside the endosome or lysosome, covalently attached payloads are released and subsequently diffuse to regions of the cell (for example, the nucleus or cytosol) to perform their MoA. Graphic created with BioRender.com.

https://doi.org/10.1038/s41587-025-02772-z

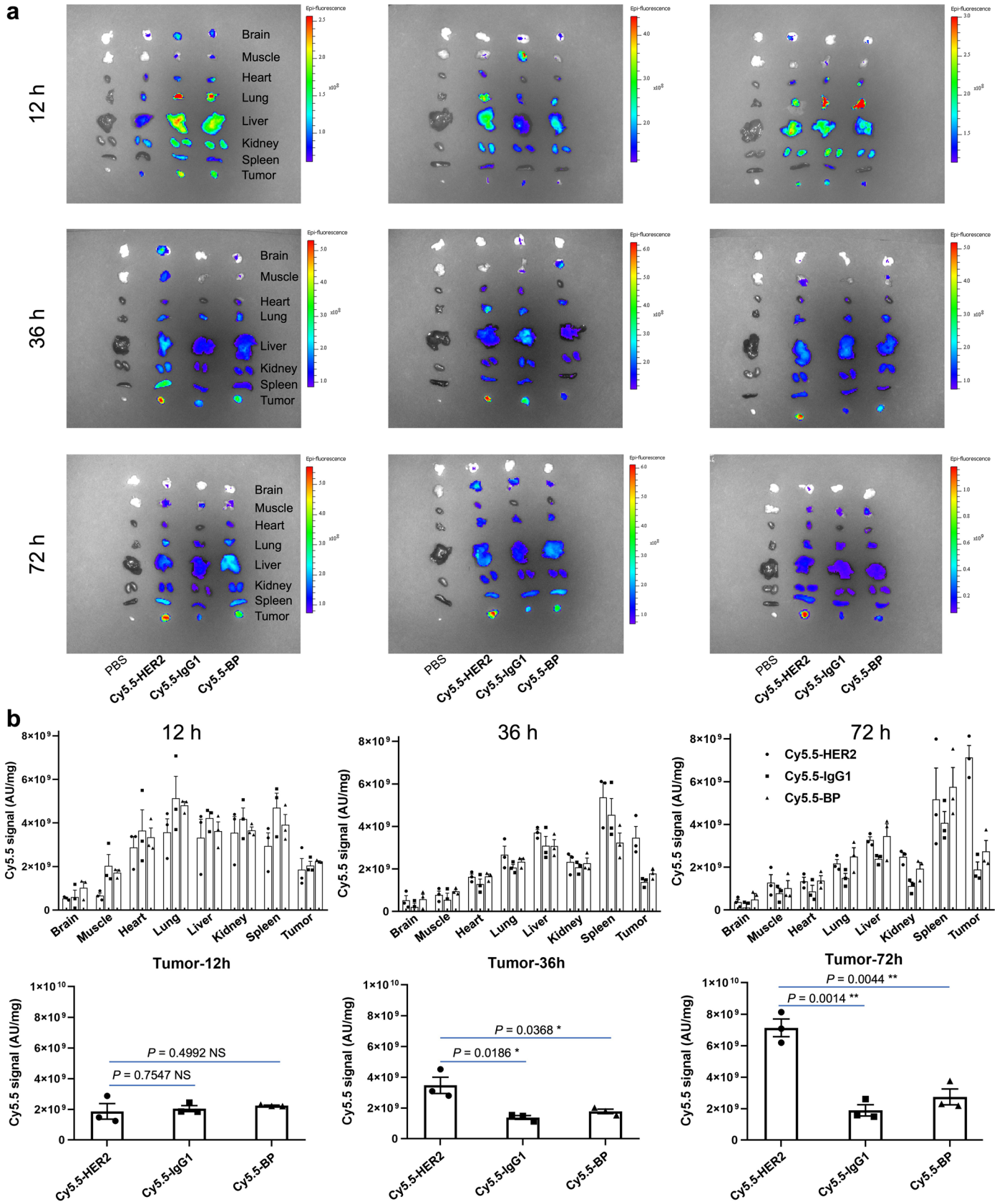

Extended Data Fig. 7 | Time-dependent biodistribution (BD) studies. **a**. *Ex vivo* images of organs from mice ($n = 3$) at different time points following administration of Cy5.5-HER2 and non-targeted controls Cy5.5-IgG1 and Cy5.5-BP. **b**. Quantification of time-dependent BD for targeted and non-targeted constructs as quantified by fluorescence imaging. The bottom bar graphs correspond to the tumor fluorescence signals for different treatment groups, showing substantially greater tumor accumulation for HER2-targeting Cy5.5-HER2. Results are presented as mean ± SEM ($n = 3$ biological replicates). Statistical analysis was done using a 2-tailed *t*-test. For these statistical tests, NS denotes non-significant; *, $P < 0.05$; **, $P < 0.01$.

https://doi.org/10.1038/s41587-025-02772-z

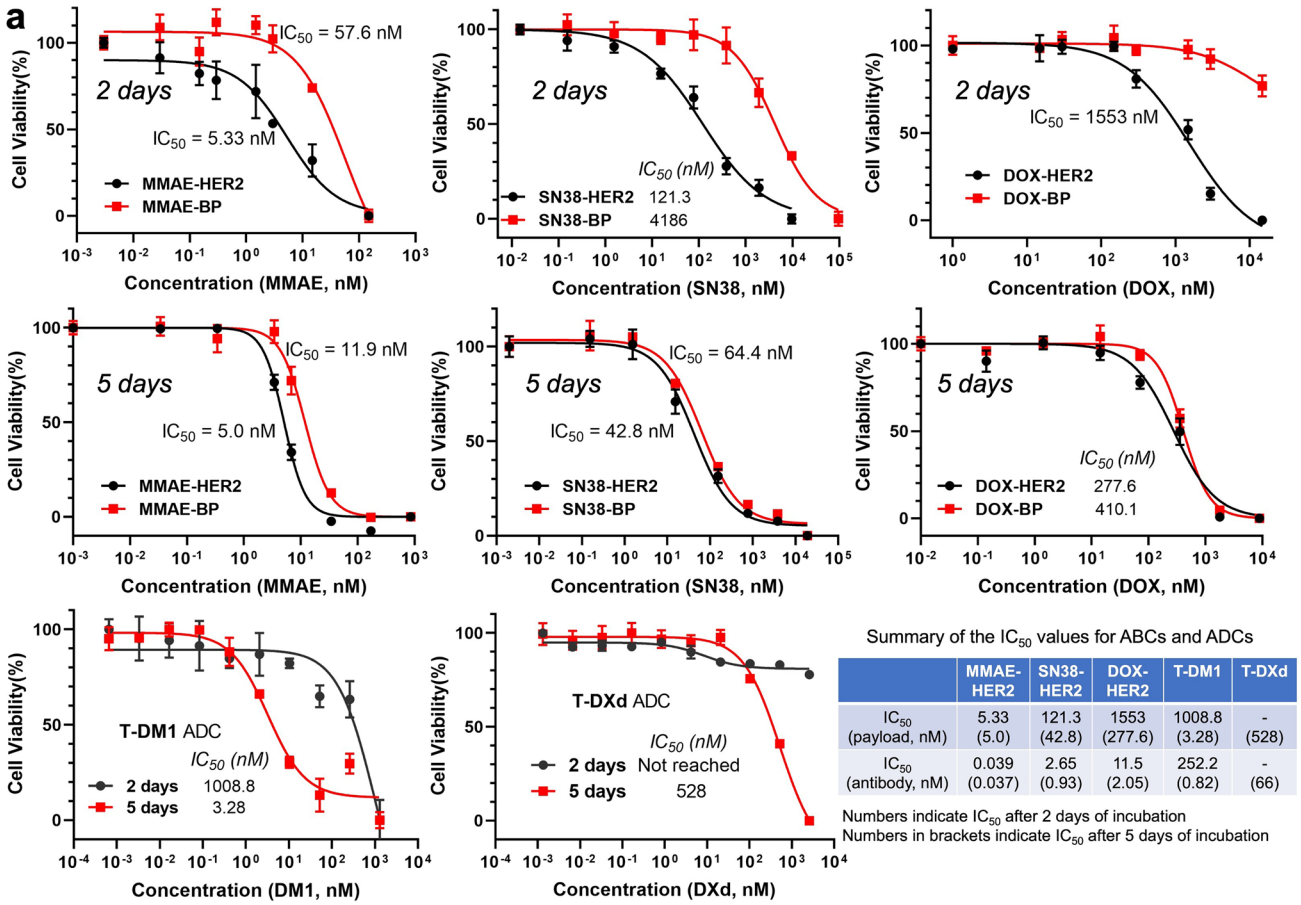

Summary of the IC_{50} values for ABCs and ADCs

	MMAE-HER2	SN38-HER2	DOX-HER2	T-DM1	T-DXd
IC_{50} (payload, nM)	5.33 (5.0)	121.3 (42.8)	1553 (277.6)	1008.8 (3.28)	- (528)
IC_{50} (antibody, nM)	0.039 (0.037)	2.65 (0.93)	11.5 (2.05)	252.2 (0.82)	- (66)

Numbers indicate IC_{50} after 2 days of incubation
Numbers in brackets indicate IC_{50} after 5 days of incubation

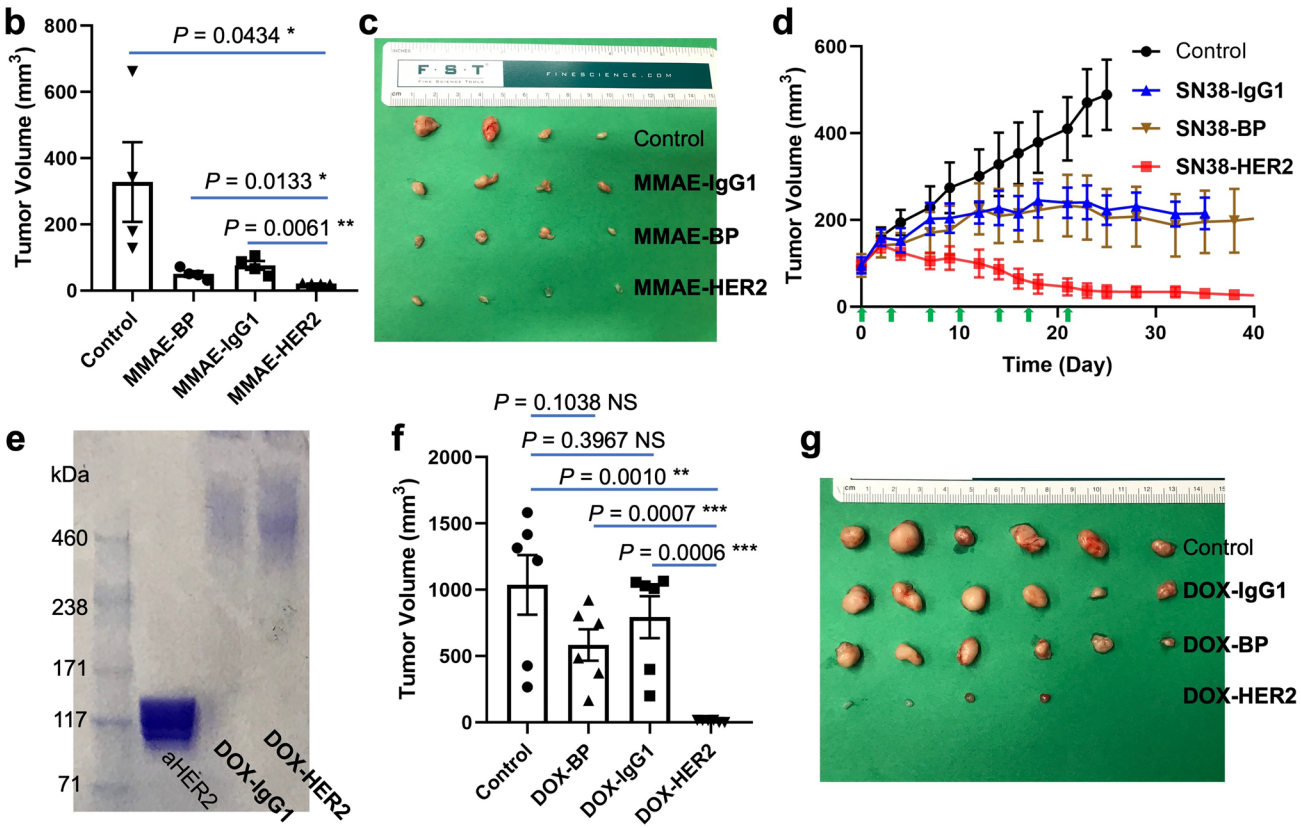

Extended Data Fig. 8 | See next page for caption.

https://doi.org/10.1038/s41587-025-02772-z

Extended Data Fig. 8 | In vitro and in vivo evaluation of the anticancer efficiency of ABCs with different payloads on BT-474 cells or xenograft tumor model. a. Cell viability studies for ABCs with different payloads compared to their nontargeting BPs (top and middle row, from left to right: MMAE, SN-38, and DOX; top row: 2 days incubation; bottom row: 5 days incubation) and different ADCs (bottom row, from left to right: T-DM1 and T-DXd, 2 d or 5 d incubation). Each data point represents the mean of three independent replicates ($n = 3$ biological replicates). **b**. BT-474 tumor volumes at day 40 for mice given MMAE-based ABCs and non-targeted controls ($n = 4$ mice/group). **c**. *Ex vivo* images of the tumors at day 40 for mice given MMAE-based constructs. **d**. Enlarged Fig. 3d for tumor volume measurement with dose schedule illustrated via green arrows ($n = 6$ mice/group). **e**. SDS-PAGE analysis of ABCs with DOX as the payload. **f**. BT-474 tumor volumes at day 40 for mice given DOX-based ABCs and non-targeted controls ($n = 6$ mice/group). **g**. *Ex vivo* images of the tumors at day 40 for mice given DOX-based constructs. Results are presented as mean ± SEM. Statistical analysis was done using a 2-tailed *t*-test. For these statistical tests, NS denotes non-significant; *, $P < 0.05$; **, $P < 0.01$.

https://doi.org/10.1038/s41587-025-02772-z

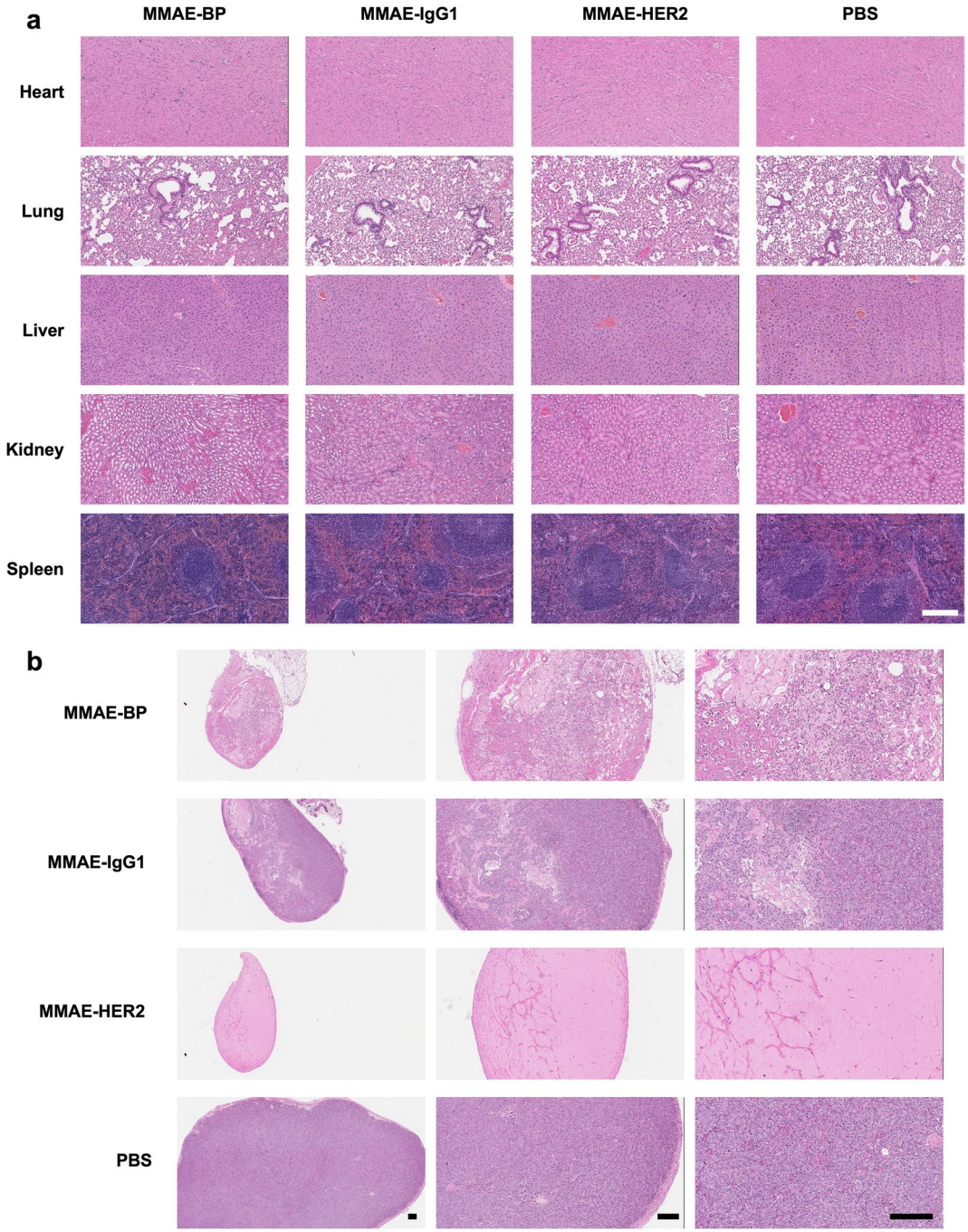

Extended Data Fig. 9 | Images of mice organs and xenografts examined after ABC treatments in the BT-474 xenograft tumor model. Tissue sections were formalin-fixed paraffin-embedded (FFPE), stained with hematoxylin and eosin (H&E), and evaluated by a board-certified veterinary pathologist. **a**. No sign of toxicity was observed in the heart, lung, liver, spleen, and kidney, supporting a good safety profile. **b**. Xenografts with different magnifications. Tumor cells were only visible in the PBS, MMAE-BP, and MMAE-IgG1 groups. Tumor-bearing mice were treated with MMAE-based constructs (5 mg/kg mAb; 1.7 mg/kg MMAE per dose). Mice were dosed once a week for a total of 4 doses as illustrated via green arrows in panel a of Fig. 3. Scale bar = 300 μm. For each representative histology image, tissue sections from 4 mice were analyzed independently, with 3 slices examined per mouse, yielding similar results across all samples.

nature portfolio

Corresponding author(s): Jeremiah A. Johnson

Last updated by author(s): Jun 17, 2025

Reporting Summary

Nature Portfolio wishes to improve the reproducibility of the work that we publish. This form provides structure for consistency and transparency in reporting. For further information on Nature Portfolio policies, see our Editorial Policies and the Editorial Policy Checklist.

Statistics

For all statistical analyses, confirm that the following items are present in the figure legend, table legend, main text, or Methods section.

n/a	Confirmed
☐	☒ The exact sample size (*n*) for each experimental group/condition, given as a discrete number and unit of measurement
☐	☒ A statement on whether measurements were taken from distinct samples or whether the same sample was measured repeatedly
☐	☒ The statistical test(s) used AND whether they are one- or two-sided *Only common tests should be described solely by name; describe more complex techniques in the Methods section.*
☐	☒ A description of all covariates tested
☐	☒ A description of any assumptions or corrections, such as tests of normality and adjustment for multiple comparisons
☐	☒ A full description of the statistical parameters including central tendency (e.g. means) or other basic estimates (e.g. regression coefficient) AND variation (e.g. standard deviation) or associated estimates of uncertainty (e.g. confidence intervals)
☐	☒ For null hypothesis testing, the test statistic (e.g. *F*, *t*, *r*) with confidence intervals, effect sizes, degrees of freedom and *P* value noted *Give P values as exact values whenever suitable.*
☒	☐ For Bayesian analysis, information on the choice of priors and Markov chain Monte Carlo settings
☒	☐ For hierarchical and complex designs, identification of the appropriate level for tests and full reporting of outcomes
☒	☐ Estimates of effect sizes (e.g. Cohen's *d*, Pearson's *r*), indicating how they were calculated

Our web collection on statistics for biologists contains articles on many of the points above.

Software and code

Policy information about availability of computer code

Data collection	Bruker Topspin 4.0 (NMR), Agilent ChemStation Rev. B. 04 03-SP1 (87) (LC-MS), Bruker Daltonics FlexAnalysis 3.4 (MALDI-TOF-MS), Wyatt Dynamics 7.5.0.17 (DLS), Wyatt ASTRA 6.1 (GPC), SpectraMax M3 (UV absorbance, fluorescence, and cell toxicity assays), Perkin Elmer Living Image 4.5 (IVIS), BD FACSDiva V9.0 (flow cytometry), Gatan Microscopy Suite Digital Micrograph 2.32.888.0 (cryo-EM)
Data analysis	OriginPro 8, Persus V 2.0.7.0, BioGRID V 4.4.237, and GraphPad Prism (V 8.1.0 & V 9.5) for data analysis and plotting; MestReNova v12.0.4 for NMR analysis; Perkin Elmer Living Image 4.5 for in vivo imaging analysis; Flowjo (V 10.9) for flow cytometry analysis; msAxel 1.0.5.2 for HR-MS analysis.

For manuscripts utilizing custom algorithms or software that are central to the research but not yet described in published literature, software must be made available to editors and reviewers. We strongly encourage code deposition in a community repository (e.g. GitHub). See the Nature Portfolio guidelines for submitting code & software for further information.

Data

Policy information about availability of data

All manuscripts must include a data availability statement. This statement should provide the following information, where applicable:

- Accession codes, unique identifiers, or web links for publicly available datasets
- A description of any restrictions on data availability
- For clinical datasets or third party data, please ensure that the statement adheres to our policy

All data supporting the findings of this study are available within the Article, its Supplementary Information, on Figshare (doi:10.6084/m9.figshare.29414048), and can be obtained from the corresponding authors upon reasonable request.

Research involving human participants, their data, or biological material

Policy information about studies with human participants or human data. See also policy information about sex, gender (identity/presentation), and sexual orientation and race, ethnicity and racism.

Reporting on sex and gender	This research did not involve any human participants.
Reporting on race, ethnicity, or other socially relevant groupings	N/A
Population characteristics	N/A
Recruitment	N/A
Ethics oversight	N/A

Note that full information on the approval of the study protocol must also be provided in the manuscript.

Field-specific reporting

Please select the one below that is the best fit for your research. If you are not sure, read the appropriate sections before making your selection.

☒ Life sciences ☐ Behavioural & social sciences ☐ Ecological, evolutionary & environmental sciences

For a reference copy of the document with all sections, see nature.com/documents/nr-reporting-summary-flat.pdf

Life sciences study design

All studies must disclose on these points even when the disclosure is negative.

Sample size	In vitro studies were done with n = 3/group, affording statistically significant means and standard deviations. In vivo studies were done with n= 4-8/group for each condition, affording statistically significant means and standard deviations.
Data exclusions	No data was excluded from the studies presented in this work.
Replication	In vitro studies were done in 2 biological replicates. All attempts at replication were successful. In vivo studies were not replicated.
Randomization	Mice are randomized into study groups at the start of all studies. For in vitro studies, samples were randomly grouped for each experimental condition.
Blinding	In vitro and in vivo studies were blinded (researcher does not know the identity of study groups, mice are blinded by default).

Reporting for specific materials, systems and methods

We require information from authors about some types of materials, experimental systems and methods used in many studies. Here, indicate whether each material, system or method listed is relevant to your study. If you are not sure if a list item applies to your research, read the appropriate section before selecting a response.

Materials & experimental systems

n/a	Involved in the study
☐	☒ Antibodies
☐	☒ Eukaryotic cell lines
☒	☐ Palaeontology and archaeology
☐	☒ Animals and other organisms
☒	☐ Clinical data
☒	☐ Dual use research of concern
☒	☐ Plants

Methods

n/a	Involved in the study
☒	☐ ChIP-seq
☐	☒ Flow cytometry
☒	☐ MRI-based neuroimaging

Antibodies

Antibodies used

All the antibodies in this study were purchased from commercial suppliers. Trastuzumab (Catalog #SIM0005, Clone: Trastuzumab), IgG1 (Catalog #CP174), and anti-MUC1 (Catalog #BE0336,Clone: C595 (NCRC48)) were purchased from BioXCell. IgG (from human serum, Catalog #I4506-50MG) was purchased from Sigma. The site-specific thiol-engineered Trastuzumab antibody was manufactured by Biointron Biological USA Inc. via substitution of a glutamic acid in the heavy chain with a cysteine. Peroxidase AffiniPure Goat Anti-Human IgG (Jackson ImmunoResearch) was used as the secondary antibody.

Validation

All the antibodies are from commericial sources. The validation of the antibodies had been conducted by the supplier and they were not further validated. The purity of all the antibodies was greater than 95% as determined by the supplier via SDS-PAGE. Anti-HER2 (Trastuzumab, RRID: AB_2894726) antibody was validated for use in research. Validation data confirms that this clone binds to its target antigen and the validation information is available on the manufacturer's website. Anti-MUC1(RRID: AB_2894756) has been shown to suppress ovarian tumor xenograft growth in mice. Validation information is available on the manufacturer's website. IgG from human serum was used as a standard in SDS-PAGE. IgG1 isotype control antibody reacts with hen egg lysozyme and has low or no specific binding to any human sample.

Eukaryotic cell lines

Policy information about cell lines and Sex and Gender in Research

Cell line source(s)

BT474 (ATCC, clone 5), HCC-70 (ATCC), SKBR-3(ATCC), SKOV-3(ATCC), MCF10A(ATCC), CAOV-3(ATCC)

Authentication

None of the cell lines were authenticated other then by morphology.

Mycoplasma contamination

All cell lines tested negative for mycoplasma contamination.

Commonly misidentified lines
(See ICLAC register)

No commonly misidentified cell lines were used in the study.

Animals and other research organisms

Policy information about studies involving animals; ARRIVE guidelines recommended for reporting animal research, and Sex and Gender in Research

Laboratory animals

NCR nude mice (8-12 weeks old)

Wild animals

No wild animals were used in the study.

Reporting on sex

Only female mice were used in this study, owing to the fact that male mice may fight more with each other, especially when carrying diseases such as cancer.

Field-collected samples

No field-collected samples were used in the study.

Ethics oversight

All experiments involving animals were reviewed and approved by the the MIT Committee for Animal Care (CAC).

Note that full information on the approval of the study protocol must also be provided in the manuscript.

Plants

Seed stocks	*Report on the source of all seed stocks or other plant material used. If applicable, state the seed stock centre and catalogue number. If plant specimens were collected from the field, describe the collection location, date and sampling procedures.*
Novel plant genotypes	*Describe the methods by which all novel plant genotypes were produced. This includes those generated by transgenic approaches, gene editing, chemical/radiation-based mutagenesis and hybridization. For transgenic lines, describe the transformation method, the number of independent lines analyzed and the generation upon which experiments were performed. For gene-edited lines, describe the editor used, the endogenous sequence targeted for editing, the targeting guide RNA sequence (if applicable) and how the editor was applied.*
Authentication	*Describe any authentication procedures for each seed stock used or novel genotype generated. Describe any experiments used to assess the effect of a mutation and, where applicable, how potential secondary effects (e.g. second site T-DNA insertions, mosiacism, off-target gene editing) were examined.*

Flow Cytometry

Plots

Confirm that:

☒ The axis labels state the marker and fluorochrome used (e.g. CD4-FITC).

☒ The axis scales are clearly visible. Include numbers along axes only for bottom left plot of group (a 'group' is an analysis of identical markers).

☒ All plots are contour plots with outliers or pseudocolor plots.

☒ A numerical value for number of cells or percentage (with statistics) is provided.

Methodology

Sample preparation	Detailed sample preparation are shown in the Method..
Instrument	BD FACSymphony A3
Software	The software FACSDiva (v.9.0) from respective instrument was used to acquire the data. FlowJo (v.10.9) was used for data analysis.
Cell population abundance	We used at least 10,000 cell counts for each sample.
Gating strategy	Dead cells were excluded based on Zombie Yellow staining, and viable cells of interest were further analysed for cell uptake quantification.

☒ Tick this box to confirm that a figure exemplifying the gating strategy is provided in the Supplementary Information.